

## This is to certify that the thesis entitled

2000

### COMPUTATIONAL STUDY OF HEAT AND MASS TRANSFER WITH PHASE CHANGE CONDENSATION AND EVAPORATION IN A DEVELOPING, TWO-DIMENSIONAL WALL JET VELOCITY AND TEMPERATURE FIELDS

presented by

R. Arman Dwiartono

has been accepted towards fulfillment of the requirements for the

M.S.	degree in	Department of Mechanical Engineering
Cia	iW_	Lama A
	Major Prof	essor's Signature
	8	/20/2004
		Date

MSU is an Affirmative Action/Equal Opportunity Institution

## LIBRARY Michigan State University

PLACE IN RETURN BOX to remove this checkout from your record.

TO AVOID FINES return on or before date due.

MAY BE RECALLED with earlier due date if requested.

DATE DUE	DATE DUE
	DATE DUE

6/01 c:/CIRC/DateDue.p65-p.15

# COMPUTATIONAL STUDY OF HEAT AND MASS TRANSFER WITH PHASE CHANGE CONDENSATION AND EVAPORATION IN A DEVELOPING, TWO-DIMENSIONAL WALL JET VELOCITY AND TEMPERATURE FIELDS

Ву

R. Arman Dwiartono

### **A THESIS**

Submitted to
Michigan State University
in partial fulfillment of the requirements
for the degree of

MASTER OF SCIENCE

Department of Mechanical Engineering

2004

### **ABSTRACT**

COMPUTATIONAL STUDY OF HEAT AND MASS TRANSFER WITH PHASE CHANGE CONDENSATION AND EVAPORATION IN A DEVELOPING, TWO-DIMENSIONAL WALL JET VELOCITY AND TEMPERATURE FIELDS

Ву

### R. Arman Dwiartono

One of the important aspects of this study is to predict condensation and evaporation during window defogging or defrosting that happens in certain temperatures. The safety issue to defrost or defog in a short period of time is a main concern in automotive industry to avoid any hazard that could happen to drivers. The government also regulates this safety issue.

A 2-D steady state and transient computational simulation with phase change modeling with the implementation of User Defined Function were performed with FLUENT as the commercial code to be compared with the experimental study that was done previously.

It was determined later that in predicting the window defogging, Sherwood Number plays as an important role. Results of this computational study were in good agreement with the experimental and other study regarding window defogging that was done previously. This study shows that computational simulation could be applied successfully to investigate condensation and evaporation for the window defogging or defrosting problem.

To my parents, brother, and Eliza

#### ACKNOWLEDGMENT

I wish to express my deepest thanks to my graduate advisor, Dr. Craig Somerton, for his time, constant support and helpful advice throughout my entire program. He was always available whenever I needed his help.

To my committee members, Bashar AbdulNour Ph.D., Paul Hoke Ph.D., and Dr. Andre Benard I would like to say my thanks to them, they also help me with their advice and assistance. They spent their time to help and taught me with their knowledge and experience in this subject. This research will not be as useful without the previous experiment done by Dr. Paul Hoke, Mr. Qingtian Wang, Dr. Bashar AbdulNour, and few other people. I would like to thank them for their valuable resources for this research. Dr. AbdulNour and Dr. Paul Hoke of Ford Motor Company have the confidence in me and continue to support me in the technical field to do this research during my program.

Finally, I would like to thank my friends, family, and Eliza for their support to keep me going. They always gave me moral boost and kept my confidence high.

### **TABLE OF CONTENTS**

List of Tables	<b>v</b> i
List of Figures	<b>v</b> ii
Nomenclature	<b>x</b>
Introduction	1
CHAPTER 1. Background investigation and review of literature	2
1.1 BACKGROUND INVESTIGATION	4
CHAPTER 2. Numerical methodology 2.1 DESCRIBING EQUATIONS AND BOUNDARY CONDITIONS 2.1.1 WALL REGION $0 \le y \le \delta_w$ AND $0 \le x \le L$	9
2.1.2 WATER LAYER REGION $\delta_w \le y \le \delta_t$ AND $0 \le x \le L$	12
2.3 FINITE VOLUME METHOD	21 21 23
CHAPTER 3. Steady state and transient simulation 3.1 STEADY-STATE INITIAL CONDITION 3.2 STEADY-STATE RESULTS AND DISCUSSION 3.3 UNSTEADY-STATE INITIAL CONDITION 3.4 UNSTEADY-STATE RESULTS AND DISCUSSION	.26 28 41
CHAPTER 4. CONCLUSIONS AND FUTURE WORK	.55
APPENDIX A. User defined function for the volumetric phase charmodel	nge 59

APPENDIX B. User defined function for the volumetric phase change (without mass source)	ge model 63
APPENDIX C. Residual Plot of 2-D Steady State Run	67
APPENDIX D. Computational Results	68
BIBLIOGRAPHY	73

### LIST OF TABLES

Chapter 3	
Table 3.1. Initial condition inputted for inlet and outlet of the mode	l28
Table D.1. Condensation Rate with Only Diffusion	68
Table D.2. Condensation Rate with Only Convection	68
Table D.3. Condensation Rate with Convection and Diffusion	68
Table D.4. Reynolds and Sherwood Number for Condensation	69
Table D.5. Reynolds and Sherwood Number for Evaporation	69
Table D.6. Reynolds Number for Transient	69
Table D.7. Liquid Layer Thickness vs. Time for Different           Number	

### **LIST OF FIGURES**

Chapter 1	
Figure 1.1. FMTF Experimental Setup	3
Chapter 2	
Figure 2.1. Physical Model	g
Figure 2.2. Geometry of the Model with Mesh	18
Figure 2.3. Detail of the Model	19
Figure 2.4. Two-Dimensional FVM Grid	22
Chapter 3	
Figure 3.1.1. Flow Field (m/s) of Air Region	29
Figure 3.1.2. Zoom View of Flow Field (m/s) of Air Region	29
Figure 3.2. Comparison of Velocity Magnitude with Previous Study	31
Figure 3.3. Temperature vs. Position at Different x/w Location	32
Figure 3.4.1. Concentration Field (kg/m³) in Air Region	33
Figure 3.4.2. Zoom View of Concentration Field (kg/m³) in Air Region	33
Figure 3.5.1. Comparison of Condensation Rate with Experimental Data	34
Figure 3.5.2. Comparison of Condensation Rate with Previous  Computational Results	. 35
Figure 3.6. Comparison of Condensation and Evaporation at Liquid Layer Interface	36
Figure 3.7. Condensation Rates Due to Diffusion and Convection	37

Figure 3.8. Local Sherwood Number vs. Local Reynolds Number38
Figure 3.9. Sherwood Number vs. Reynolds Number40
Figure 3.10. Liquid Layer Thickness vs. Time at Different Reynolds Number
Figure 3.11.1. Velocity Flow Field after 5 Seconds In Unsteady-Simulation46
Figure 3.11.2. Zoom View of Velocity Flow Field after 5 Seconds46
Figure 3.12.1. Present Study of Condensation Thickness vs. Time48
Figure 3.12.2. Condensation Thickness vs. Time from Previous Study48
Figure 3.13.1. Mass Flow Rate vs. Time Step at x/w = 1.5949
Figure 3.13.2. Mass Flow Rate vs. Time for Different x/w50
<b>Figure 3.14.1.</b> Local Sherwood Number vs. Time at x/w = 3.1851
Figure 3.14.2. Local Sherwood Number vs. Time at Different x/w52
Figure 3.15. Reynolds Number vs. Time Step53
*Images in this thesis are presented in color

### **NOMENCLATURE**

A Area (m<sup>2</sup>)

C<sub>o</sub> Specific Heat at Constant Pressure (J/kg-K)

D Mass diffusivity (m<sup>2</sup>/s)

D<sub>eff</sub> Effective Diffusion Coefficient (m<sup>2</sup>/s)

DNS Direct Numerical Simulation

E Total Energy (J/m<sup>3</sup>)

E<sub>v</sub> Voltage Output (V)

FMTF Ford-MSU Test Facility

h Heat Transfer Coefficient (W/m²-K)

h<sub>m</sub> Mass Transfer Coefficient (m/s)

J Mass flux (kg/m²-s)

k Thermal Conductivity (W/m-k)

k<sub>eff</sub> Effective Thermal Conductivity (W/m-k)

k-ε Kinetic Energy and dissipation rate

Le Lewis Number

L Latent Heat (Kj/kg)

m Mass (kg)

 $m_{\nu}$  Volumetric mass flow rate of water vapor (kg/m<sup>3</sup>-s)

P<sub>sat</sub> Saturation Pressure (Pa)

P Pressure (Pa)

P<sub>v</sub> Partial Pressure of vapor in mixture (Pa)

₹:

Pr Prandtl Number

q" Heat Flux (W/m²)

R Gas Constant (kJ/kg-K)

Re Reynolds Number

Rey Turbulent Reynolds Number

Rew Reynolds Number based on jet nozzle width

Rh Relative Humidity (%)

RMS Root Mean Square

RSM Reynold Stress Model

S Source Term

S<sub>m</sub> Source Term in the mass continuity equation (kg/m³-s)

Sc Schmidt Number

Sh Sherwood Number

SNS Streamwise Normal Stress

T Temperature (°C or K)

T<sub>dp</sub> Dew Point Temperature (°C or K)

T<sub>jet</sub> Temperature at the jet nozzle (°C or K)

T<sub>ref</sub> Reference Temperature (°C or K)

t Time (s)

u,v,w Velocity component in x,y,z direction (m/s)

 $u_{v}, v_{v}$  x and y velocity components of water vapor (m/s)

U Velocity magnitude (m/s)

U<sub>jet</sub> Velocity at the jet nozzle (m/s)

17 19 10 1 1 1 1 1

To a Charman Property of

And the second of the second

$U_{\sf max}$	Maximum velocity magnitude (m/s)
$U_{\tau}$	Friction Velocity (m/s)
u'	RMS velocity (m/s)
w	Width of the jet nozzle (m)
X	Mole Fraction
	Greek
α	Thermal Diffusivity (m²/s)
β	Coefficient of Thermal Expansion
Δ	Delta
$\delta_2$	y location where velocity magnitude equals U/2
3	Eddy Diffusivity (m²/s)
ф	Relative Humidity
Φ	Mass Fraction
μ	Dynamic Viscosity (kg/s-m)
μ	Turbulent Viscosity (kg/s-m)
ν	Kinematic Viscosity (m²/s)
ρ	Density (kg/m³)
$\rho_{\mathbf{w}}$	Mass concentration at the wall (kg/m³)
τij	Stress Tensor (Pa)
ω	Specific Humidity (kg H <sub>2</sub> O/kg air)

Contact Est

 $\Re (\mathcal{P}(\chi) + 2 \chi (\ell))$ 

## Subscripts

- 9 Non-condensable gas
- liquid
- v Vapor
- w Wall

### INTRODUCTION

This study concerns condensation and evaporation of water from a vertical surface in the presence of wall jet flow field. The CFD software package FLUENT has been used to develop a computational solution to the problem. The domain of interest has been specified to be consistent with an experimental rig (Ford-MSU Test Facility) that was previously used to generate results [1]. This allows direct comparison between the numerical results and experimental results. The motivation for this study is to develop a predictive model that can be used to design windshield defrosting and defogging systems. In the automotive industry, window defrosting and defogging are major safety issues and key customer concerns. Impaired driver visibility due to inadequate window defogging has been shown to be a constant concern and is regulated by the Federal Government. Motor vehicles need to defrost and defog the windshield over short periods of time in order to avoid any hazards, delays for the driver, and additional fogging and condensation.

#### **CHAPTER 1**

## BACKGROUND INVESTIGATION AND REVIEW OF LITERATURE

## 1.1 BACKGROUND INVESTIGATION

The following section outlines the experiment that has been done previously through FMTF (Ford-MSU Test Facility) by Paul Hoke. The measurement, data acquisition, and motion control was done experimentally in the test facility. Later, the result of this experimental will be compared to the computer simulation result that has been done through Fluent.

A wall jet is defined by Launder and Rodi [2] as a shear flow directed along a wall. As a first step in doing defogging research, the angle of this wall is set initially at zero degree.

Defogging would be best described as corrective action using the flow of air over the windshield. Because of the complexity of the defrosting mechanisms and to simplify the defrost duct design, the best approach is to use CFD with the established boundary conditions.

The fluid studied in the window defogging experiment is a mixture of water and non-condensable air. The numerical simulation includes investigation of velocity field, turbulence quantities, and the temperature field. Since the plate surface temperature is adjustable, a phase change of condensation or evaporation will occur under certain thermal circumstances. Modeling the

transient phenomenon with valid Sherwood Number becomes very important in the continuing study of this field.

Following is the schematic of the experimental setup:

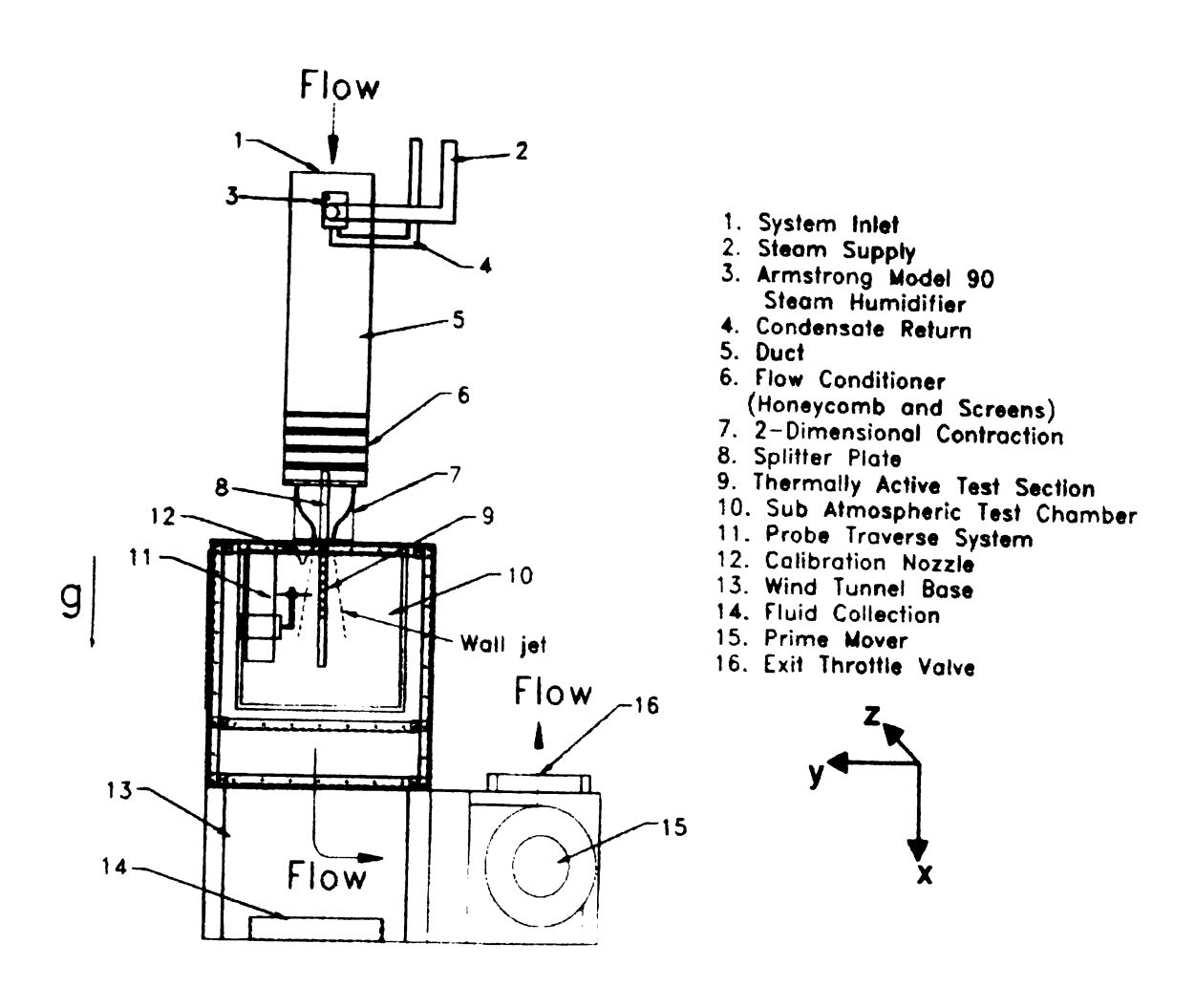


Figure 1.1. FMTF Experimental Setup

The region of interest for the experimental investigations is mainly the thermally active test section, indicated by label 9 in the above figure. The thermally active test plate is an aluminum heat exchanger with an interchangeable faceplate. The driving force for the whole system is the pressure

differential between label 1 (system inlet) and label 13 (wind tunnel base) that was created by label 15 (the prime mover). The fluid studied was mixture of water and non-condensable air.

Since the plate surface temperature T<sub>s</sub> is adjustable, a phase change condensation or evaporation of water will occur under certain thermal circumstances. This condensation and evaporation phenomena is the main concern in the windshield defogging issue. Hence, investigating the phase change model became very necessary topic.

The task to simulate wall jet is not simple, considering the phase change with heat and mass transfer that occur along the process. The goal of the current research is to computationally determine the condensation and evaporation that occurs and then optimize the windshield-defogging model.

### 1.2 BACKGROUND EQUATIONS

By using Fluent, some of the equations have been tackled in the computer. However, Fluent does not have the equations needed to model phase change condensation or evaporation. We need to input these equations through a UDF (User Defined Function) or by inputting the equation through the CFF (Custom Field Function). Mainly, a UDF is used throughout the iteration while the CFF is more for the post-processing results.

Following is the continuity equation that is solved by Fluent:

$$\frac{\partial \rho}{\partial t} + \frac{\partial}{\partial x_i} (\rho u_i) = S \tag{1.1}$$

This general form of continuity equation is valid for both compressible and incompressible flows.

For the phase change process, the UDF is attached in the Appendix A and Appendix B.

To measure the condensation rate, the formula inputted to the CFF is as follow:

$$M = \overline{J_w} * A * 60 Seconds \tag{1.2}$$

Where J<sub>w</sub> is the mass flux of the wall that was calculated:

$$\overline{J_{w}} = \left[ \frac{(\rho_{g} + \rho_{v})^{2}}{\rho_{g} \rho_{v}} D \frac{\partial}{\partial y} \left( \frac{\rho_{g}}{\rho_{g} + \rho_{v}} \right) \right]_{w}$$
(1.3)

The water vapor mass flux at the wall is related to the diffusional velocity. As the gaseous components are assumed to be perfect, the  $\rho_g/(\rho_g+\rho_v)$  gradient is directly related to the partial pressure gradient dp<sub>v</sub>/dT multiplied by the temperature gradient dT/dy. Hence, the mass flux of the water vapor and total heat transfer are known as soon as the temperature and concentration gradients at the wall are known.

### 1.3 REVIEW OF LITERATURE

Little previous work has been done regarding momentum and heat transfer associated with a wall jet in the presence of the phase change. Hoke [1] performed an experimental study of heat transfer and condensation in a developing, two-dimensional wall jet flow field with an isothermal boundary condition. The experimental results from this study serve as a benchmark for comparison with the computational results of present study. The parameters of

this computational study were set so as to agree with the data or the experimental study. Launder and Rodi [2] provide a compilation of studies involving the flow of a two-dimensional jet over flat surfaces and surfaces with a variety of profiles, pressure gradients, free stream velocities, and initial jet turbulence intensities. All these results are summarized in *The Turbulent Wall Jet* [2].

Previous work regarding condensation in laminar and turbulent boundary layers includes Legay-Desesquelles and Prunet-Foch [3]. They considered heat and mass transfer with condensation in laminar and turbulent boundary layers along a flat plate. Several of their models are used in the numerical calculation for the present study. Their assumptions included that the volume of the condensed droplets in the gaseous boundary layer is negligible, the liquid film is so thin that it can be neglected in terms of heat transfer, and there is no interaction between droplets. To study condensation heat transfer in both laminar and turbulent boundary layers, Legay-Desesquelles and Prunet-Foch, determined the distribution profiles of the variables through a step by step finite difference numerical method. The mathematical model and numerical calculation offered in the Legay-Desesquelles and Prunet-Foch paper is also valid for mixture of air and water vapor, which is the subject of this study of condensation and evaporation.

AbdulNour [4] performed a CFD simulation of a model wall jet flow for defogging and defrosting. The objective of the computation was to investigate fogging of automotive glass interior surfaces and predict the flow field within the

Ford-MSU Test Facility [1], in order to evaluate the applicability of CFD to model demisting and defogging problems. The results of this study also provide a set of benchmarks for the development of simulation models in the present study.

The local heat transfer coefficients for isothermal and uniform heat flux boundary conditions for a planar wall jet have been determined experimentally [5]. Hot-wire anemometry surveys were used to quantify the velocity field in the wall jet. A micro-thermocouple was used to quantify the temperature field in the wall jet for the isothermal boundary condition. The results are for non-dimensional streamwise locations that are relevant to automotive windshield defogging/defrosting, which serves as the technological motivation for this study.

For condensation and evaporation, many problems involving non-condensable gases have multiple non-condensable species, for example, air (with nitrogen, oxygen, and other gases). P.F. Peterson [6] studied this problem and presents a fundamental analysis of the mass transport with multiple non-condensable species, identifying a simple method to calculate an effective mass diffusion coefficient that can be used with the simple diffusion layer model.

Siow et al. [7] present results for laminar film condensation of vapor-gas mixtures in horizontal flat-plate channels using a fully coupled implicit numerical approach that achieves excellent convergence behavior. These results correspond to steam-air and R134a-air mixtures over wide ranges of the parameters. Effects of the four independent variables (inlet values of gas concentration, Reynolds number and pressure, and the inlet-to-wall temperature difference) on the film thickness, pressure gradient, and the local and average

Nusselt numbers are carefully examined. It was found that the condensation of R134a-air corresponds to thicker liquid films, lower heat transfer rates, and lower algebraic values of the pressure gradient when compared with steam-air at the same operating conditions.

Hassan et al. [8] performed windshield-defogging simulation. Though their purpose is similar to the present study, their mathematical model and numerical calculation are different than used here. This literature also serves as a reference base and comparison between experimental and computational results. Accuracy of results in both experimental and computational studies plays a significant role. Hence, when results are compared they should have significant agreement.

This thesis continues with a presentation of the governing equations and boundary conditions for the physical model. The use of FLUENT to solve these equations is then discussed. Next, results are provided and are shown to be consistent with the physical understanding of the processes at work. The use of these results to predict window defogging, conclusions, and recommendations complete the paper.

### **CHAPTER 2**

### **NUMERICAL METHODOLOGY**

### 2.1 DESCRIBING EQUATIONS AND BOUNDARY CONDITIONS

The physical situation modeled in this problem is shown in Figure 2.1. Three physical regions are identified, each with their own set of describing equations: the wall, water layer, and air chamber. The describing equations and boundary conditions are presented for each region below.

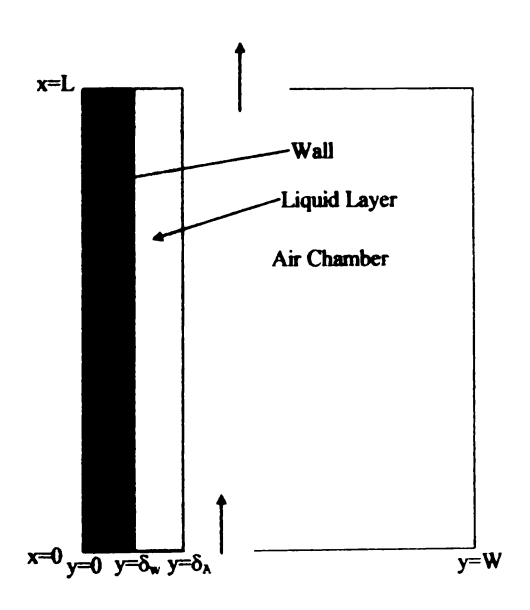


Figure 2.1. Physical Model

## 2.1.1 WALL REGION $0 \le y \le \delta_w$ and $0 \le x \le L$

The only conservation equation of importance is the energy equation, given by

$$\frac{\partial^2 T_w}{\partial x^2} + \frac{\partial^2 T_w}{\partial y^2} = 0$$
 (2.1)

(Only conduction in the two dimensions of interest have been included)

The thermal boundary and matching conditions are

$$\left. \frac{\partial T_{\mathbf{w}}}{\partial \mathbf{y}} \right|_{\mathbf{y} = \mathbf{0}} = \mathbf{0} \tag{2.2a}$$

(adiabatic back surface)

$$k_{w} \frac{\partial T_{w}}{\partial y} \bigg|_{y=\delta_{w}} = k_{\ell} \frac{\partial T_{\ell}}{\partial y} \bigg|_{y=\delta_{w}}$$
 (2.2b)

(matching of heat flux at wall-liquid layer interface)

$$T_{w}(y = \delta_{w}) = T_{\ell}(y = \delta_{w})$$
 (2.2c)

(matching of temperature at wall-liquid layer interface)

$$\left. \frac{\partial T_{w}}{\partial y} \right|_{x=0} = 0 \tag{2.2d}$$

(adiabatic bottom surface)

$$\left. \frac{\partial T_{\mathbf{w}}}{\partial \mathbf{y}} \right|_{\mathbf{x} = \mathbf{L}} = 0 \tag{2.2e}$$

(adiabatic top surface)

## 2.1.2 WATER LAYER REGION $\delta_{w} \le y \le \delta_{t}$ and $0 \le x \le L$

It has been assumed that there is no flow in the water, so that the only conservation equation of importance is the energy equation. Then

$$\frac{\partial^2 T_{\ell}}{\partial x^2} + \frac{\partial^2 T_{\ell}}{\partial y^2} = 0 \tag{2.3}$$

(only conduction in the two dimensions of interest have been included)

The thermal boundary and matching conditions are

$$k_{w} \frac{\partial T_{w}}{\partial y} \bigg|_{y = \delta_{w}} = k_{\ell} \frac{\partial T_{\ell}}{\partial y} \bigg|_{y = \delta_{w}}$$
(2.4a)

(matching of heat flux at wall-liquid layer interface)

$$T_{w}(y = \delta_{w}) = T_{\ell}(y = \delta_{w})$$
(2.4b)

(matching of temperature at wall-liquid layer interface)

$$k_{\ell} \frac{\partial T_{\ell}}{\partial y} \bigg|_{y = \delta_{\ell}} = k_{a} \frac{\partial T_{a}}{\partial y} \bigg|_{y = \delta_{\ell}} + \dot{m}_{cond}^{"} \hat{h}_{fg}$$
 (2.4c)

(matching of heat flux with phase change at liquid layer-air chamber interface)

$$T_{\ell}(y = \delta_{\ell}) = T_{a}(y = \delta_{\ell})$$
 (2.4b)

(matching of temperature at liquid layer-air chamber interface)

$$\left. \frac{\partial \Gamma_{\ell}}{\partial y} \right|_{x=0} = 0 \tag{2.4e}$$

(adiabatic bottom surface)

$$\left. \frac{\partial T_{\ell}}{\partial y} \right|_{x=L} = 0 \tag{2.4f}$$

(adiabatic top surface)

## 2.1.3 AIR CHAMBER REGION $\delta_\ell \le y \le W$ and $0 \le x \le L$

### **Continuity Equation:**

$$\frac{\partial}{\partial x}(\rho u) + \frac{\partial}{\partial y}(\rho v) = S_m \tag{2.5}$$

where 
$$S_m = \frac{\partial}{\partial x} \left[ \rho \Phi \left( u - \frac{1}{\Phi} D \frac{\partial}{\partial x} (\Phi) \right) \right] + \frac{\partial}{\partial y} \left[ \rho \Phi \left( v - \frac{1}{\Phi} D \frac{\partial}{\partial y} (\Phi) \right) \right]$$
 (2.6)

## Momentum Equation:

$$\frac{\partial}{\partial x}(\rho uu) = -\frac{\partial p}{\partial x} + \frac{\partial \tau}{\partial x} + \rho g \tag{2.7a}$$

$$\frac{\partial}{\partial y}(\rho uu) = -\frac{\partial p}{\partial y} + \frac{\partial \tau}{\partial y}$$
 (2.7b)

p is the static pressure,  $\rho g$  is the gravitational body force, and  $\tau$  is the stress tensor. The stress tensor is given by

$$\tau = \tau_{newtonian} + \tau_{turbulent}$$
 (2.8a)

Where

$$\tau_{newtonian} = -P\delta_{ij} + \mu \left( \frac{\partial u}{\partial x} + \frac{\partial v}{\partial y} \right)$$
 (2.8b)

$$\tau_{turbulent} = -\rho u'v' \tag{2.8c}$$

### **Energy Equation:**

$$\frac{\partial}{\partial x} [u(\rho E + p)] + \frac{\partial}{\partial y} [v(\rho E + p)] =$$

$$\left\{ \frac{\partial}{\partial x} \left[ k_{eff} \frac{\partial T}{\partial x} - \sum hJ + u(\tau)_{eff} \right] + \frac{\partial}{\partial y} \left[ k_{eff} \frac{\partial T}{\partial y} - \sum hJ + v(\tau)_{eff} \right] \right\} + S_h$$
(2.9)

Where E is the total energy

$$E = h - \frac{p}{\rho} + \frac{u^2}{2}$$
 (2.10)

For ideal gas, the boundary condition with j as the species for the enthalpy is:

$$h = \sum_{j} \Phi_{j} h_{j} \tag{2.11}$$

The density follows the value for ideal gas, while the thermal conductivity, viscosity, and specific heat are 0.0261 W/m-K, 1.5647\*10<sup>-5</sup> kg/m-s, and 1510.21 J/kg-K, respectively.

The equation with  $\tau_{\text{eff}}$  represents the viscous heating.  $\tau_{\text{eff}}$  is the deviatory stress tensor given by:

$$\tau_{eff} = \mu_{eff} \left( \frac{\partial u}{\partial x} + \frac{\partial v}{\partial y} \right) - \frac{2}{3} \mu_{eff} \frac{\partial u}{\partial x} \delta$$
 (2.12)

The effective thermal conductivity is

$${}^{k}eff^{=k+k}t \tag{2.13}$$

Where the turbulent thermal conductivity is

$$k_t = \frac{c_p \mu_t}{\Pr_t} \tag{2.14}$$

In realizable k- $\epsilon$  model, the turbulent viscosity is

$$\mu_t = \rho C_{\mu} \frac{k^2}{\varepsilon} \tag{2.15}$$

In this case,

$$C_{\mu} = \frac{1}{A_0 + A_s \frac{Uk}{E}} \tag{2.16}$$

The boundary condition for A<sub>0</sub> and A<sub>s</sub> is given by

$$A_0 = 4.04 A_s = \sqrt{6}\cos\phi$$
 (2.17)

### **Mass Species Equation:**

$$\frac{\partial}{\partial x}(\rho u \Phi) + \frac{\partial}{\partial y}(\rho v \Phi) = \left[ \frac{(\rho_g + \rho_v)^2}{\rho_g \rho_v} D \frac{\partial}{\partial y} \left( \frac{\rho_g}{\rho_g + \rho_v} \right) \right]$$
(2.18)

In turbulent flows, the mass diffusion flux is

$$J = -\left(\rho D + \frac{\mu_t}{Sc_t}\right) \frac{\partial \Phi}{\partial x}$$
 (2.19a)

Where

$$Sc_{t} = \frac{\mu_{t}}{\rho D_{t}}$$
 (2.19b)

For turbulent Schmidt number, the boundary condition is a default value of 0.7,  $\mu_t$  is the turbulent eddy viscosity, and  $D_t$  is the effective diffusion coefficient due to turbulence.

The thermal boundary and matching conditions are

$$u(x, y = \delta_{\ell}) = 0$$
 (2.20a)

(no slip condition)

$$u(x, y = W) = 0$$
 (2.20b)

(no slip condition)

$$u(x = 0, \delta_{\ell} \le y \le w) = u_{jet}$$
 (2.20c)

(jet inlet)

$$u(x = 0, w \le y \le W) = 0$$
 (2.20d)

(kinematic condition)

$$u(x = L, \delta_{\ell} \le y \le w_{exit}) = \frac{w}{w_{exit}} \cdot u_{jet}$$
 (2.20e)

(jet exit)

$$u(x = 1, w_{exit} \le y \le W) = 0$$
 (2.20f)

(kinematic condition)

$$v(x, y = \delta_{\ell}) = 0$$
 (2.21a)

(kinematic condition)

$$V(x, y = W) = 0$$
 (2.21b)

(kinematic condition)

$$v(x = 0, y) = 0$$
 (2.21c)

(no slip condition)

$$v(x = L, y) = 0$$
 (2.21d)

(no slip condition)

$$P(x = 0, y) = P_0$$
 (2.22a)

(static condition)

$$P(x, y = \delta_{\ell}) = 0$$
 (2.22b)

(static condition)

$$\mathbf{k}_{\ell} \frac{\partial \Gamma_{\ell}}{\partial \mathbf{y}} \bigg|_{\mathbf{y} = \delta_{\ell}} = \mathbf{k}_{\mathbf{a}} \frac{\partial \Gamma_{\mathbf{a}}}{\partial \mathbf{y}} \bigg|_{\mathbf{y} = \delta_{\ell}} + \dot{\mathbf{m}}_{\text{cond}}^{"} \hat{\mathbf{h}}_{fg}$$
 (2.23a)

(matching of heat flux with phase change at liquid layer-air chamber interface)

$$T_{\ell}(y = \delta_{\ell}) = T_{a}(y = \delta_{\ell}) \tag{2.23b}$$

(matching of temperture at liquid layer-air chamber interface)

$$\left. \frac{\partial T_{\mathbf{a}}}{\partial \mathbf{y}} \right|_{\mathbf{y} = \mathbf{W}} = 0 \tag{2.23c}$$

(adiabatic side wall)

$$\left. \frac{\partial T_a}{\partial y} \right|_{x=L} = 0 \tag{2.23d}$$

(adiabatic top wall)

$$T_{a}(x = 0, \delta_{\ell} \le y \le w) = T_{iet}$$
 (2.23e)

(jet inlet)

$$\frac{\partial T_a}{\partial y}\bigg|_{x=0, w \le y \le W} = 0 \tag{2.23f}$$

(adiabatic bottom wall)

$$\Phi(y = \delta_{\ell}) = \Phi_{sat}(at T = T_a(y = \delta_{\ell}))$$
 (2.24a)

(equilibrium condition)

$$\left. \frac{\partial \Phi}{\partial y} \right|_{y=W} = 0 \tag{2.24b}$$

(zero mass flux side wall)

$$\left. \frac{\partial \Phi}{\partial \mathbf{y}} \right|_{\mathbf{x} = \mathbf{L}} = 0 \tag{2.24c}$$

(zero mass flux top wall)

$$\Phi(\mathbf{x} = 0, \delta_{\ell} \le \mathbf{y} \le \mathbf{w}) = \Phi_{\text{jet}}$$
 (2.24d)

(jet inlet)

$$\left. \frac{\partial \Phi}{\partial y} \right|_{x=0, w \le y \le W} = 0 \tag{2.24e}$$

(zero mass flux bottom wall)

## 2.2 METHOD OF SOLUTION

Most of the features to perform the computational study are built into the FLUENT software, including the solution of the conservation equations. However, in order to calculate such parameters as mass flux, condensation rate, evaporation rate, concentration potential, Sherwood Number, etc, equations have to be inputted manually in the *custom field function* of FLUENT. FLUENT does not include the capability to calculate condensation and evaporation rates directly. These rates are obtained by writing a subroutine (user defined function) and implementing it in FLUENT.

Once all the labeling is done, the model was exported to FLUENT where the numerical simulations were performed. Versions 6.0 and 6.1 were used for the computational study and to pre-process and post-process the model. The mesh was also adapted a few times in FLUENT based on the y<sup>+</sup>. The differences between adaptations were not noticeable, mainly because of the grid

independence. Thus, it verifies grid insensitivity of the solution. The adapted grid process resulted in a heavily clustered mesh in the area of the jet near the surface of the plate. The model consists of 62,088 quadrilateral cells. The geometry and mesh of the model is shown in Figure 2.1.



Figure 2.2. Geometry of the Model with Mesh

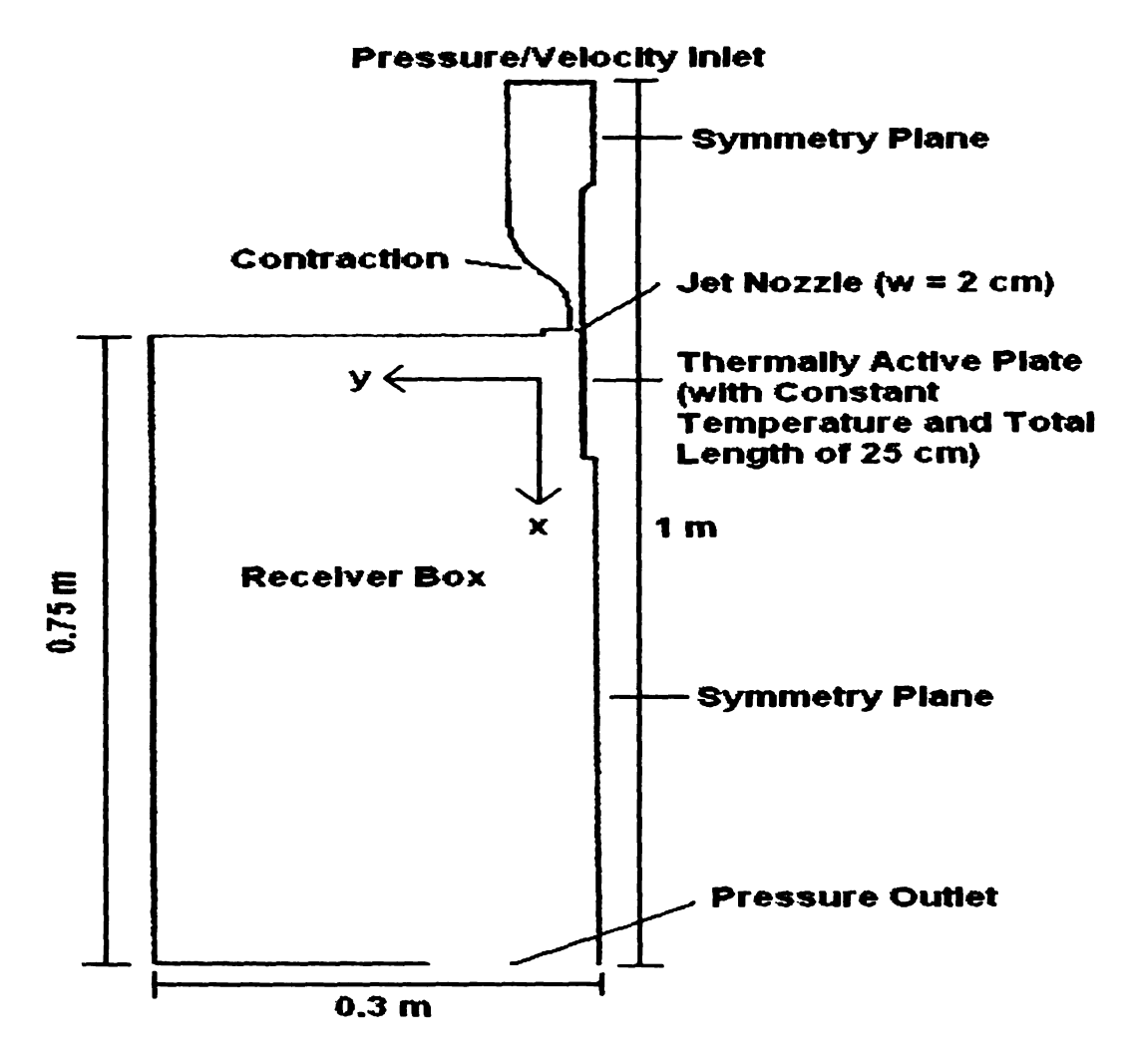


Figure 2.3. Detail of the Model

Detail of the model itself is shown in Figure 2.3. As observed, the total height of the model is 1 m with 25 cm length of the thermally active plate. The jet nozzle width is measured to be 2 cm, while the bottom exit width is 0.3 m. The model has air-water vapor flow coming in from the top, while the outlet is located at the very bottom of the model.

The contraction in the model is designed to provide a jet at the exit plane with a uniform velocity profile. The major problems in the contraction are the maintenance of good exit flow uniformity and avoidance of flow separation.

However, these problems may be solved with the criteria of a minimum nozzle length and a minimum boundary layer thickness.

This study was done in 2-D space with implicit formulation and steady time. The energy equation was also enabled during the computational run.

The turbulence model of this experiment was set as "realizable"  $k-\epsilon$ , which is a modification of standard  $k-\epsilon$ . The "realizable" designation indicates that the model satisfies certain mathematical constraints on the Reynolds (normal) stresses, which are not realizable with the standard  $k-\epsilon$  or the renormalization group (RNG) models. In FLUENT, the equation for k is derived from the solution of the approximated Reynolds-averaged Navier-Stokes equations, while the equation for  $\epsilon$  is formulated from an exact dynamic equation for the transport of the mean-square vorticity fluctuations.

The computations were performed on a UNIX-based workstation. In total, there were 591 iterations before the solution converged. The convergence criteria in FLUENT are 0.001.

The Finite Volume Method is used in FLUENT to convert the governing equations to algebraic equations that can be solved numerically. Using the Finite Volume Method instead of the Finite Difference Method allows the use of unstructured mesh, since arbitrary volumes can be utilized to divide the physical domain. This is very useful when solving a highly complicated and unstructured physical domain that would be very difficult to construct with a structured mesh.

FLUENT 6.0 and 6.1 uses internal data structures to assign order to the grid points, cells, and faces in the mesh. It also maintains the contact between

adjacent cells. In this study, the velocity, temperature, laminar, and turbulence fluctuations were predicted with the realizable k- $\epsilon$  (rke), which is part of the two equations model. A phase change model was developed to perform the mass transfer calculations. The surface phase model was implemented, resulting in water vapor condensation and evaporation.

#### 2.3 FINITE VOLUME METHOD

The finite volume method is a numerical method for solving partial differential equations that calculates the values of the conserved variables averaged across the volume. One advantage of the finite volume method over finite difference methods is that it does not require a structured mesh (although a structured mesh can also be used). Furthermore, the finite volume method is preferable to other methods as a result of the fact that boundary conditions can be applied non-invasively. This is true because the values of the conserved variables are located within the volume element, and not at nodes or surfaces. Finite volume methods are especially powerful on coarse non-uniform grids and in calculations where the mesh moves to track interfaces or shocks.

### 2.3.1 FINITE VOLUME METHOD FOR TWO-DIMENSIONAL PROBLEM

The technique for the two-dimensional steady state diffusion equation is given by:

$$\frac{\partial}{\partial x} \left( \Gamma \frac{\partial \phi}{\partial x} \right) + \frac{\partial}{\partial y} \left( \Gamma \frac{\partial \phi}{\partial y} \right) + S = 0$$
 (2.25)

A portion of the two-dimensional grid used for the discretization is shown in Figure 2.4.

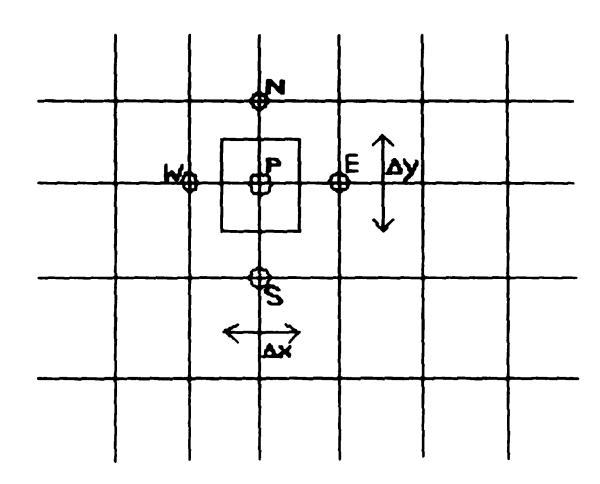


Figure 2.4. Two-Dimensional Finite Volume Method Grid

The general grid node P has east (E), west (W), north (N), and south (S) neighbors. When the above equation (2.25) is formally integrated over the control volume we obtain

$$\int_{\Delta V} \frac{\partial}{\partial x} \left( \Gamma \frac{\partial \phi}{\partial x} \right) dx.dy + \int_{\Delta V} \frac{\partial}{\partial y} \left( \Gamma \frac{\partial \phi}{\partial y} \right) dx.dy + \int_{\Delta V} S_{\phi} dV = 0$$
 (2.26)

Noting that  $A_e = A_w = \Delta y$  and  $A_n = A_s = \Delta x$ , we obtain:

$$\left[\Gamma_{e}A_{e}\left(\frac{\partial\phi}{\partial x}\right)_{e} - \Gamma_{w}A_{w}\left(\frac{\partial\phi}{\partial x}\right)_{w}\right] + \left[\Gamma_{n}A_{n}\left(\frac{\partial\phi}{\partial y}\right)_{n} - \Gamma_{s}A_{s}\left(\frac{\partial\phi}{\partial y}\right)_{s}\right] + \overline{S}\Delta V = 0 \quad (2.27)$$

This equation represents the balance of the generation of  $\Phi$  in a control volume and the fluxes through its cell faces. The distribution of the property  $\Phi$  in a given two-dimensional situation is obtained by writing discretised equations of the form:

$$a_{P}\phi_{P} = a_{W}\phi_{W} + a_{F}\phi_{F} + a_{S}\phi_{S} + a_{N}\phi_{N} + S_{U}$$
 (2.28)

Equation (2.28) is applied at each grid node of the subdivided domain. At the boundaries where the temperatures or fluxes are known the discretised equations are modified to incorporate boundary conditions in the manner of the problem.

In problems where fluid flow plays a significant role we must account for the effect of convection. Formal integration over a control volume for the steady convection-diffusion equation gives:

$$\int_{A} n.(\rho \phi u) dA = \int_{A} n.(\Gamma grad\phi) dA + \int_{CV} S_{\phi} dV$$
 (2.29)

This equation represents the flux balance in a control volume. The left hand side gives the net convective flux and the right hand side contains the net diffusive flux and the generation or destruction of the property  $\Phi$  within the control volume.

#### 2.3.2 THE CENTRAL AND UPWIND DIFFERENCING SCHEME

The central differencing approximation has been used to represent the diffusion terms. For a uniform grid, we can write the cell face values of property  $\Phi$  as

The integrated convection-diffusion equation can be written as

$$F_e \phi_e - F_w \phi_w = D_e (\phi_e - \phi_p) - D_w (\phi_P - \phi_w)$$
 (2.31)

Where.

$$F = \rho u$$
 and  $D = \frac{\Gamma}{\delta x}$  (2.32)

One of the major inadequacies of the central differencing scheme is its inability to identify flow direction. The value of property  $\Phi$  at a west cell face is always influenced by both  $\Phi_p$  and  $\Phi_w$  in central differencing. In a strongly convective flow from west to east, the above treatment is unsuitable because the west cell face should receive much stronger influencing from node W than from node P. The upwind differencing (also known as 'donor cell') differencing scheme takes into account the flow directions when determining the value at a cell face. The convected value of  $\Phi$  at a cell face is taken to be equal to the value at the upstream node. In upwind, when the flow is in the positive direction,  $u_w > 0$ ,  $u_e > 0$  ( $F_w > 0$ ,  $F_e > 0$ ), the scheme sets

$$\phi_W = \phi_W$$
 and  $\phi_P = \phi_P$  (2.33)

The discretized equation then becomes

$$F_{\rho}\phi_{P} - F_{W}\phi_{W} = D_{\rho}(F_{\rho} - \phi_{P}) - D_{W}(\phi_{P} - \phi_{W})$$
 (2.34)

The upwind differencing scheme utilizes consistent expressions to calculate fluxes through cell face; therefore it can be easily shown that the formulation is conservative.

#### 2.4 MESH GENERATION

Gambit is the software used to generate the mesh. Gambit allows us to decompose geometries for structured hex meshing or perform automated hex meshing with control over clustering. It has single interface for meshing geometry that bring together all FLUENT preprocessing in one environment. Later, the mesh was exported to FLUENT 2D version 6.0 and 6.1.

In terms of the equations, realizable k- $\epsilon$  is (r-ke) similar to standard k- $\epsilon$  (s-ke), where

$$\mu_{t} = \rho C_{\mu} \frac{k^{2}}{\varepsilon} \tag{2.35}$$

Unlike the standard k- $\epsilon$  where the  $C_\mu$  is a constant, in r-ke the  $C_\mu$  is

$$C_{\mu} = \frac{1}{A_o + A_s \frac{U^* k}{\varepsilon}} \tag{2.36}$$

Where  $A_0$  is 4.04,  $A_s$  is  $\sqrt{6}Cos\phi$ , and

$$U^{\bullet} = \sqrt{S_{\mu}S_{\mu} + \Omega_{\mu}\Omega_{\mu}} \tag{2.37}$$

 $\Omega_{ij}$  is the mean rate of rotation tensor viewed in the rotating reference frame with the angular velocity  $\omega_{k}$ . Previous works show that r-ke gives better accuracy in predicting a variety of turbulent flows result than s-ke.

## **CHAPTER 3**

# STEADY STATE AND TRANSIENT SIMULATION

## 3.1 STEADY-STATE INITIAL CONDITIONS

In order to run the iterations in Fluent, the following initial conditions were inputted for the steady-state simulation:

- 1. Solver selected: Segregated (governing equations are solved sequentially)
  - Space: 2D
  - Velocity formulation: Absolute
  - Time: Steady
  - Gradient option: Cell-based
  - Viscous: realizable k-ε
  - Near wall treatment: Enhanced wall treatment
- 2. Material selected: Water vapor (H<sub>2</sub>O) mixture with all default density, c<sub>p</sub>, thermal conductivity, viscosity, and molecular weight
- 3. Heated Plate: Temperature is set to 278.15 K (adjustable)
- 4. Inlet pressure:
  - Gauge total pressure: 0 Pa or constant velocity 1.6896 m/s
  - Temperature: 298.15 K (room temperature)
  - Direction specification method: Normal to boundary
  - Turbulence specification method: Intensity and hydraulic diameter
    - Turbulence intensity: 2.5% (measured in experiment)

- Hydraulic diameter: 0.284 m (calculated from real geometry)

## 5. Outlet Pressure:

Gauge pressure: -60 Pa

Backflow total temperature: 298.15 K

Backflow direction specification method: Normal to boundary

• Turbulence direction specification method: Intensity and hydraulic diameter

- Backflow turbulence intensity: 30%

Backflow hydraulic diameter: 0.42 m

## 6. Wall: Temperature is set to 278.15 K

For the operating condition, the pressure is set to be 1 atm (101325 Pa). This operating pressure, P<sub>op</sub>, is important for incompressible ideal gas flow since it directly determines the density. The reference pressure location can also be specified, however when pressure boundaries are involved, the reference pressure location is ignored since it is no longer needed [10]. Fluent uses gauge pressure in calculation. When absolute pressure is needed, it can be obtained with:

$$P_{abs} = P_{op} + P \tag{3.1}$$

The iteration was performed with energy equation selected. The simulation was done with second order upwind discretization to minimize numerical rounding error. The second order upwind proved to achieve better results when they are compared to the experimental data.

In order to investigate the mass transfer and condensation, a phase change UDF is also implemented as the initial condition before running the iteration.

### 3.2 STEADY-STATE RESULTS AND DISCUSSION

The default boundary condition in FLUENT is the adiabatic wall, where the heat flux equals zero. Therefore, apart from the symmetry planes, the other parameters needed for this study are:

Table 3.1. Initial Condition Inputted for Inlet and Outlet of the Model

Port	Total Press.	Temp.	Turbulent Intensity	Hydraulic Dia. (m)
	(Pa)	(K)	(%)	
Inlet	0	298.15	2.5	0.284
Outlet	-60	298.15	30	0.42

Temperature of the wall is set initially at 278.15 K, and temperature of the heated plate is also set at 278.15 K (adjustable). Results of these studies are represented through velocity, temperature, condensation, and evaporation fields Figures 3.1.1 to 3.10.

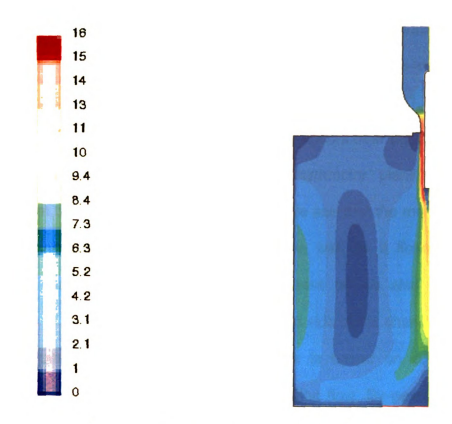


Figure 3.1.1. Flow Field (m/s) of Air Region

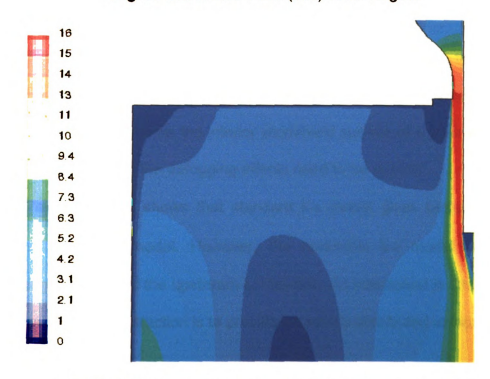


Figure 3.1.2. Zoom View of Flow Field (m/s) of Air Region

Figure 3.1.1 shows the contours of velocity after the simulation converged. The exact range of this velocity is from 0 m/s to 15.658 m/s. The more detail view of velocity contour along the thermally active plate is in Figure 3.1.2. As observed in the flow field of air region, the highest velocity occurs near the thermally active plate before decreasing along the bottom symmetry plane. The velocity distribution at the jet nozzle is nearly uniform. We see that the momentum of the jet is diffusing away from the thermally active wall as it flows through the chamber towards the outlet at the bottom. These results also show a small recirculation of the flow occurring on the left hand side of the chamber.

The principle of velocity measurements is based on convective heat transfer from a heated element to the surrounding flow. By passing an electric current through a thin metal wire, the wire temperature is higher than the ambient temperature.

The velocity distribution of the flow field is of great interest in the wall jet study. For the study of the defogger flow, more attention needs to be paid in the developing region, since on the interior windshield surface of a vehicle it is in the developing region that the defogging effects need to be applied.

Previous study shows that standard k- $\epsilon$  model gives better predictions than realizable k- $\epsilon$  model. However, the realizable k- $\epsilon$  model is better in simulating the effect of the upstream contraction. As mentioned in Chapter 2, the design purpose of contraction is to provide an evenly distributed velocity profile at the jet nozzle.

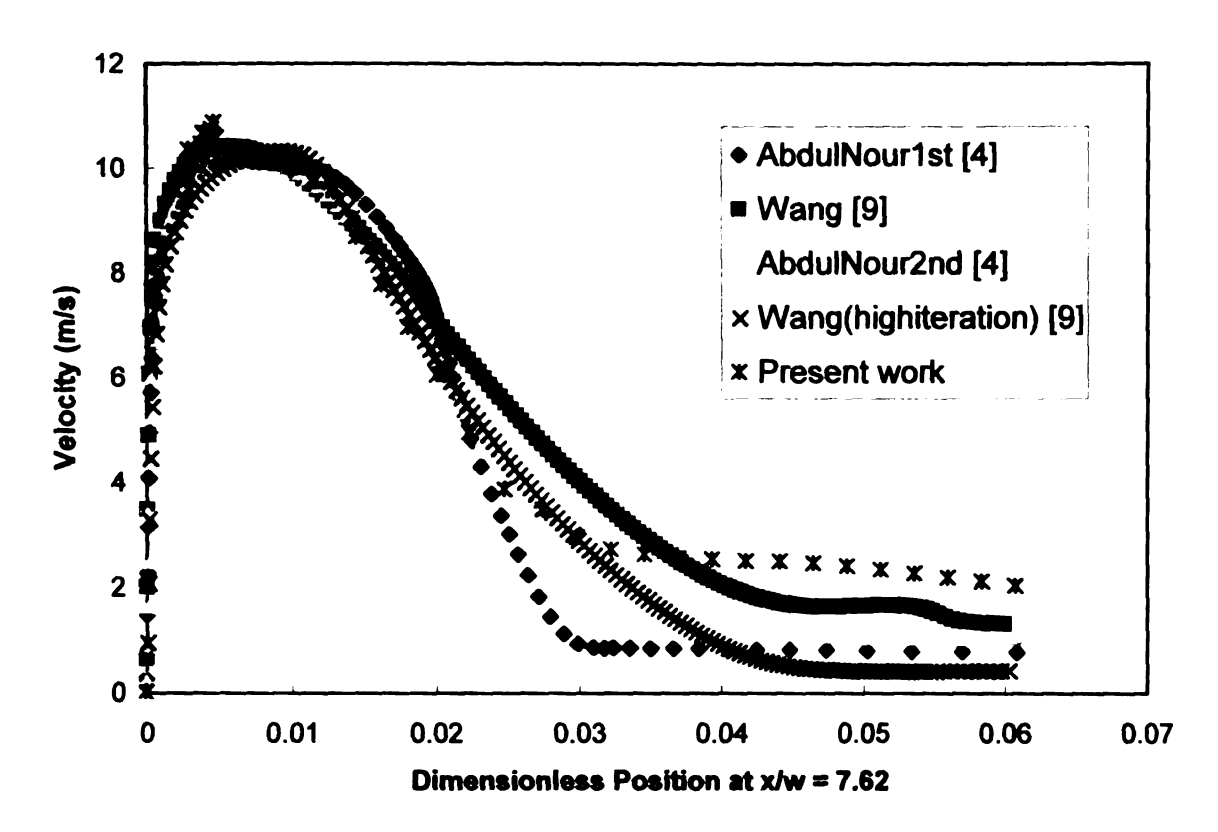


Figure 3.2. Comparison of Velocity Magnitude with Previous Study

Figure 3.2 shows the comparison of velocity magnitude at x/w = 7.62 with previous works by Wang [9] and AbdulNour [4]. As observed, the present work's result is consistent with the previous numerical work. The velocity, as expected, is highest near the wall and decreases as we move away from the wall. The present's work shows a velocity magnitude far from the wall to be higher compared to the previous studies. This may be due to a different laminar/turbulent transition point for each of the studies or over prediction of turbulent diffusion.

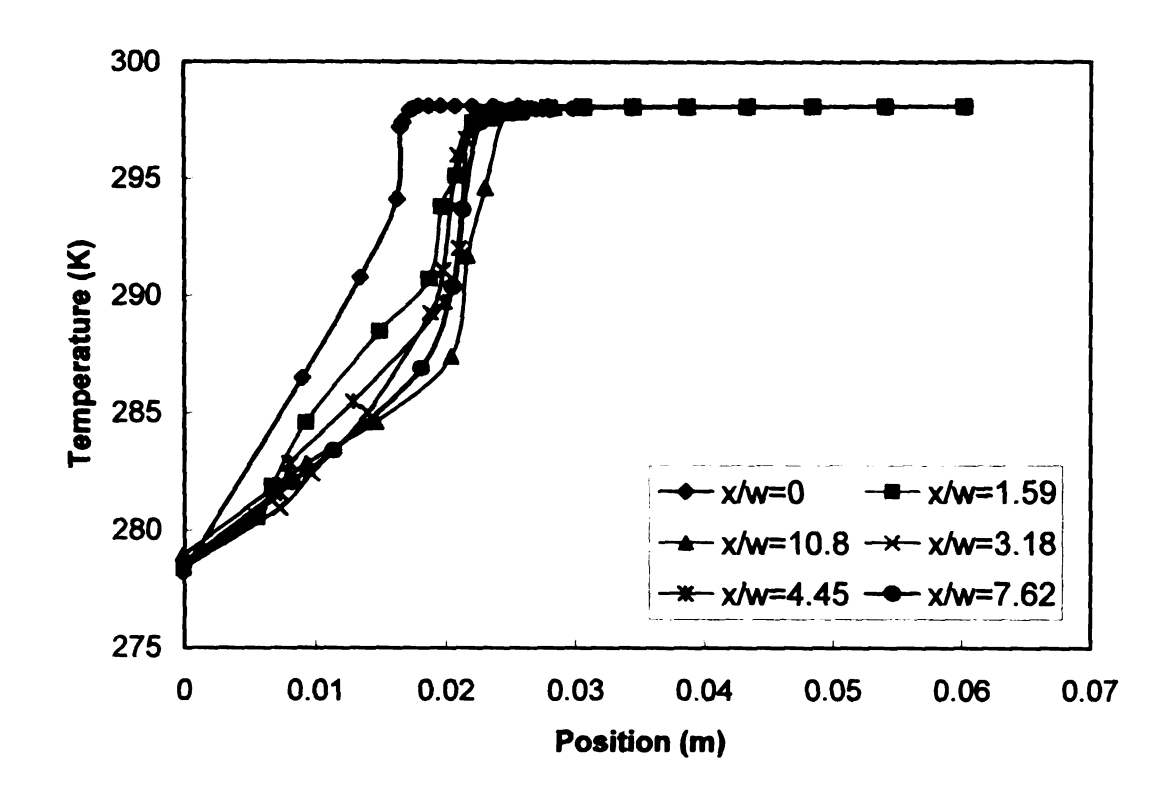


Figure 3.3. Temperature vs. Position at Different x/w Location

In Figure 3.3, the air temperature is shown against positions at various x/w locations. When x/w = 0, the respective location is at the jet nozzle. Since the inlet temperature is at 298.15 K, and temperature at the thermally active plate is at 278.15 K, this has lowest temperature. However, this rises faster with respect to the position compared to other x/w locations. As x/w gets higher, the trend is vice versa.

As we move along the plate we see significant similarity in the temperature profile, indicating that one could imply a self-similarity approach to the problem.

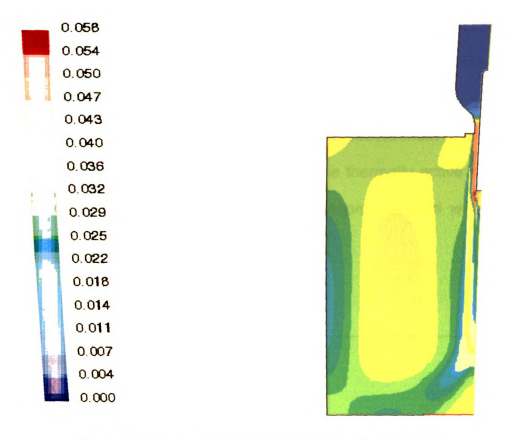


Figure 3.4.1. Concentration Field (kg/m³) in Air Region

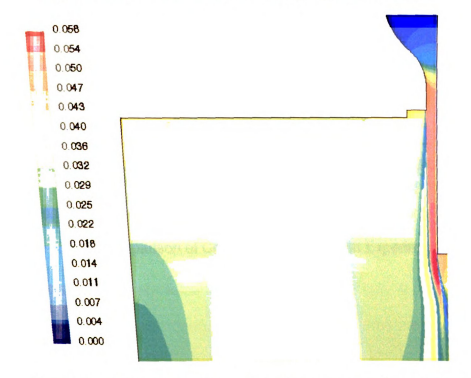


Figure 3.4.2. Zoom View of Concentration Field (kg/m³) in Air Region

Figures 3.4.1 and 3.4.2 shows the concentration field in the air region. Similar to flow field of the air region, the peak concentration decreases as the flow moves downstream along the thermally active plate. This is due to the removal of water vapor due to condensation. As expected most of the variation in concentration occurs in the air region close to the thermally active plate. Around the middle of the chamber, there is a recirculation flow field with diminished concentration potential.

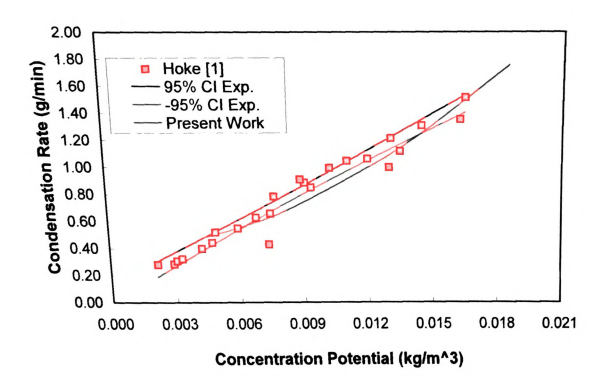


Figure 3.5.1. Comparison of Condensation Rate with Experimental Data

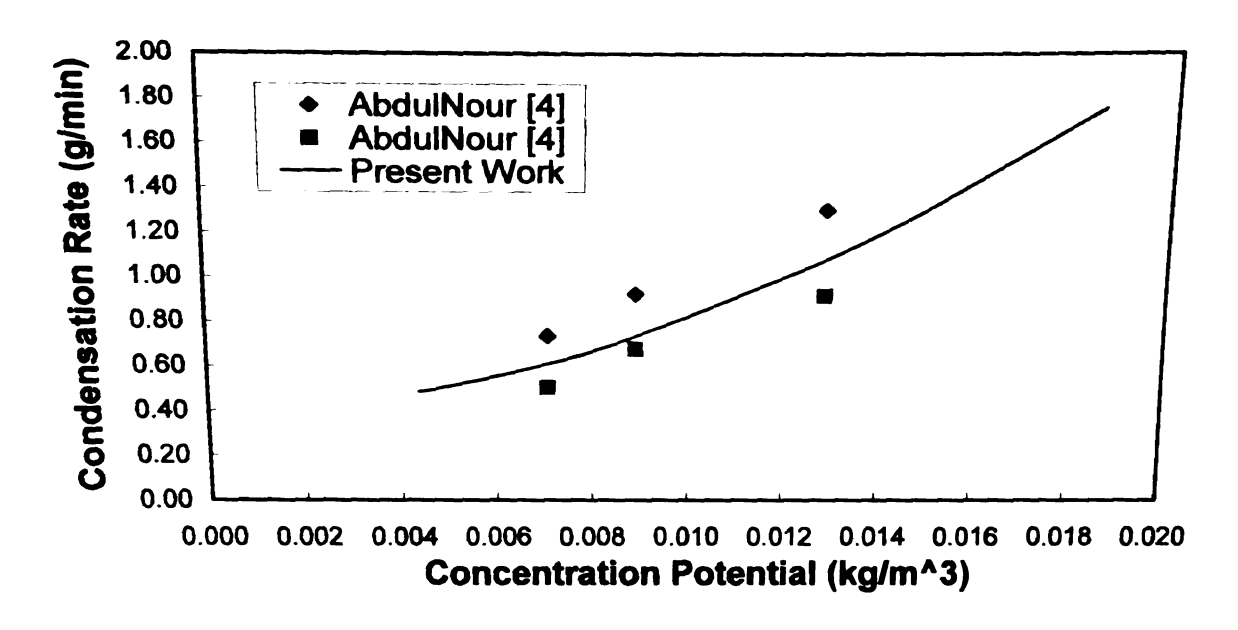


Figure 3.5.2. Comparison of Condensation Rate with Previous Computational Results

The comparison of experimental results with 95% confidential intervals and the present work is presented in Figure 3.5.1. Figure 3.5.2 shows the comparison of previous computational work with the present study. Results are presented as the condensation rate versus the concentration potential. The experimental results were provided by Hoke [1], while the numerical steady-state condensation was provided by AbdulNour et al. [5]. The numerical steady-state condensation results were calculated using FLUENT 5.0 with a User Defined Function (UDF). All the results show similar trend and range. Agreement between the computations and the experimental data (Figure 3.5.1) are fairly good, although the computation results of the present study show a somewhat smaller condensation rate. Comparisons of the results of the present study with the previous computations by AbdulNour [4] are quite good.

 $\mathcal{L}_{i}$  . The second constant  $\mathcal{L}_{i}$ 

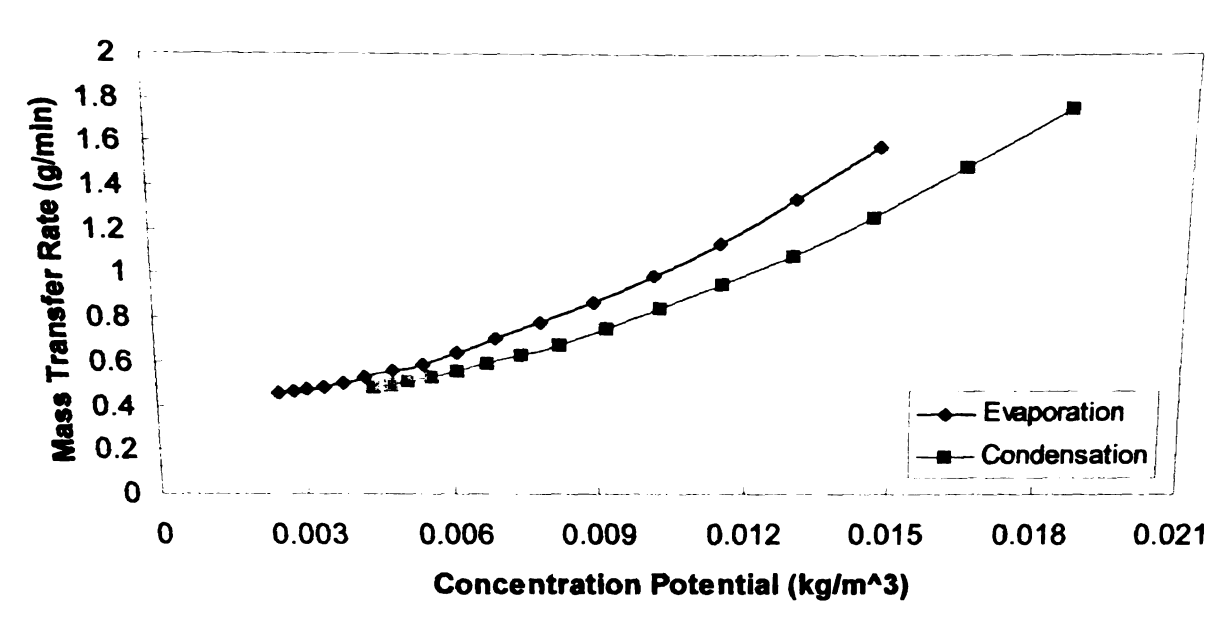


Figure 3.6. Comparison of Condensation and Evaporation at Liquid Layer Interface

Results for evaporation have also been generated. A comparison between condensation and evaporation rates can be seen in Fig. 3.6, where the evaporation rate is slightly higher rate than the condensation rate. To obtain condensation results, the inlet temperature is set higher than the thermally active plate, while for evaporation rate the setup is reversed. One might assume that the mass transfer rate should be the same for the same concentration potential whether there is condensation or evaporation. However that is not the case based on Figure 3.6.

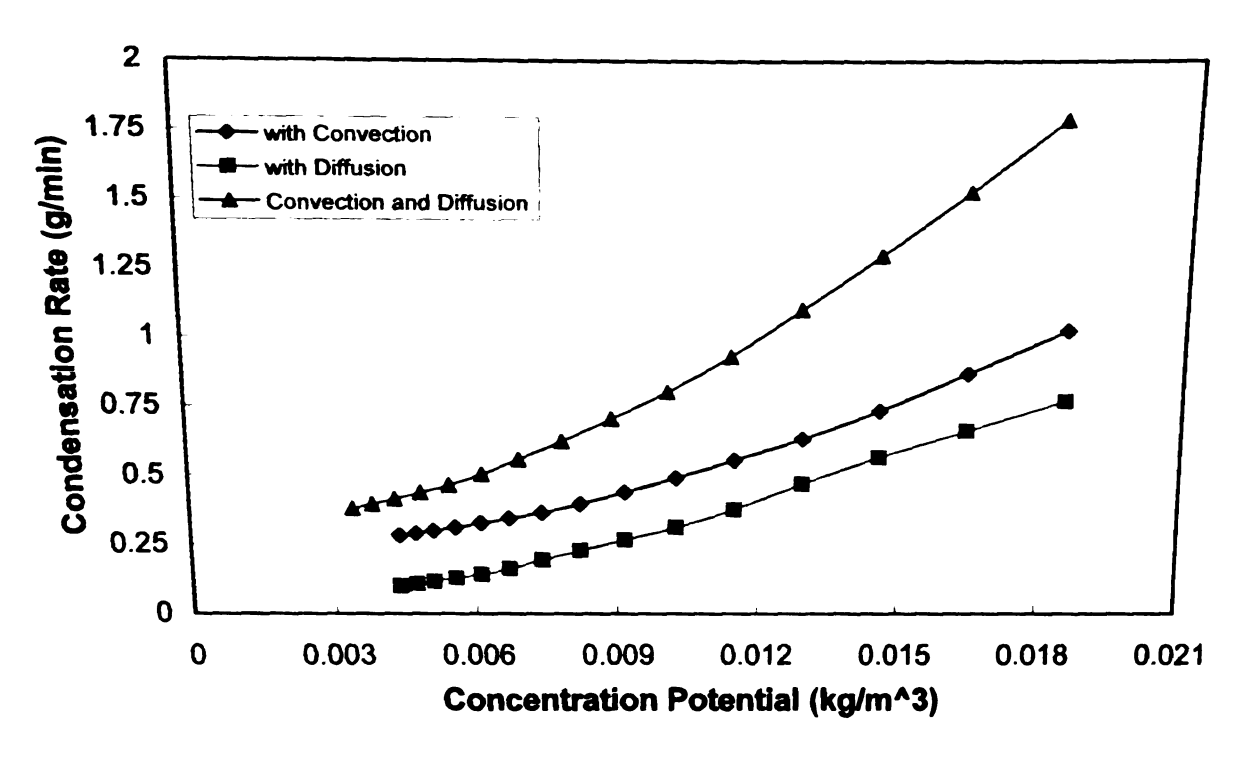


Figure 3.7. Condensation Rates Due to Diffusion and Convection

Since the condensation rate includes both diffusive and convective components, it is of interest to see how both modes contribute to the total condensation rate. This is shown in Figure 3.7. It appears that each modes contributes nearly equally to the total condensation rate, with the convective mode having a slightly greater contribution. It is clear that only including the diffusive components, as it normally done, would lead to a significant under prediction in the mass transfer.

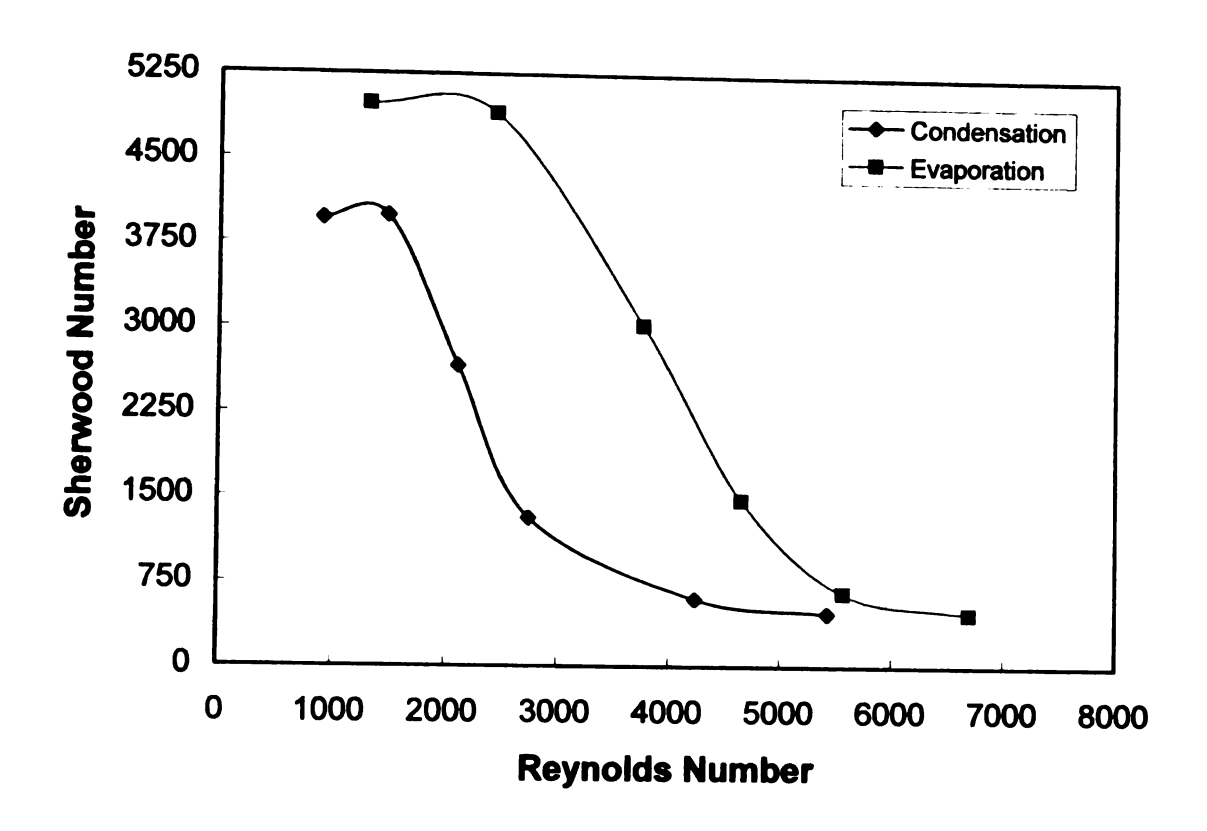


Figure 3.8. Local Sherwood Number vs. Local Reynolds Number

Figure 3.8 shows the plot of local Sherwood Number against local Reynolds Number for both condensation and evaporation. They have been defined as

$$Re_x = \frac{u_{jet}x}{v}$$
 (3.2)

$$Sh_x = \frac{Kx}{D} \tag{3.3}$$

As observed, for evaporation results, the Sherwood Number versus local Reynolds Number is higher than for the condensation results. This phenomenon could be the result of that the evaporation rate for current model is slightly higher than the condensation rate. The local Reynolds Number of a flow strongly

influences the velocity boundary layer characteristics and hence is of great importance in determining transfer coefficients. Reynolds Number is also the key parameter for determining whether flow is laminar or turbulent. The Sherwood Number can be used for future study to determine species transfer by means of correlations with windshield defogging or defrosting.

With the evidence provided above that demonstrates the ability of the computational model to predict experimental results, the steady state results can be used to develop a prediction of window defogging. A mass balance on the liquid layer gives

$$\frac{d\delta}{dt} = -\frac{K\Delta\rho_{v}}{\rho_{\ell}} \tag{3.4}$$

The initial water layer thickness of  $\delta_o$  is not a constant mass transfer coefficient, and the liquid layer temperature is changing by finite difference approximation. We find that

$$\delta(t) = \delta(t - \Delta t) - \frac{K\Delta \rho_{v}}{\rho_{t}} \Delta t \tag{3.5}$$

In order to use these results for predictive modeling, it will be useful to know the average mass transfer coefficient in terms of the jet velocity, or in dimensionless form the average Sherwood number

$$Sh_{avg} = \frac{K_{avg}L}{D} \tag{3.6}$$

In terms of jet Reynolds Number

$$\operatorname{Re}_{jet} = \frac{u_{jet}^{w}}{v} \tag{3.7}$$

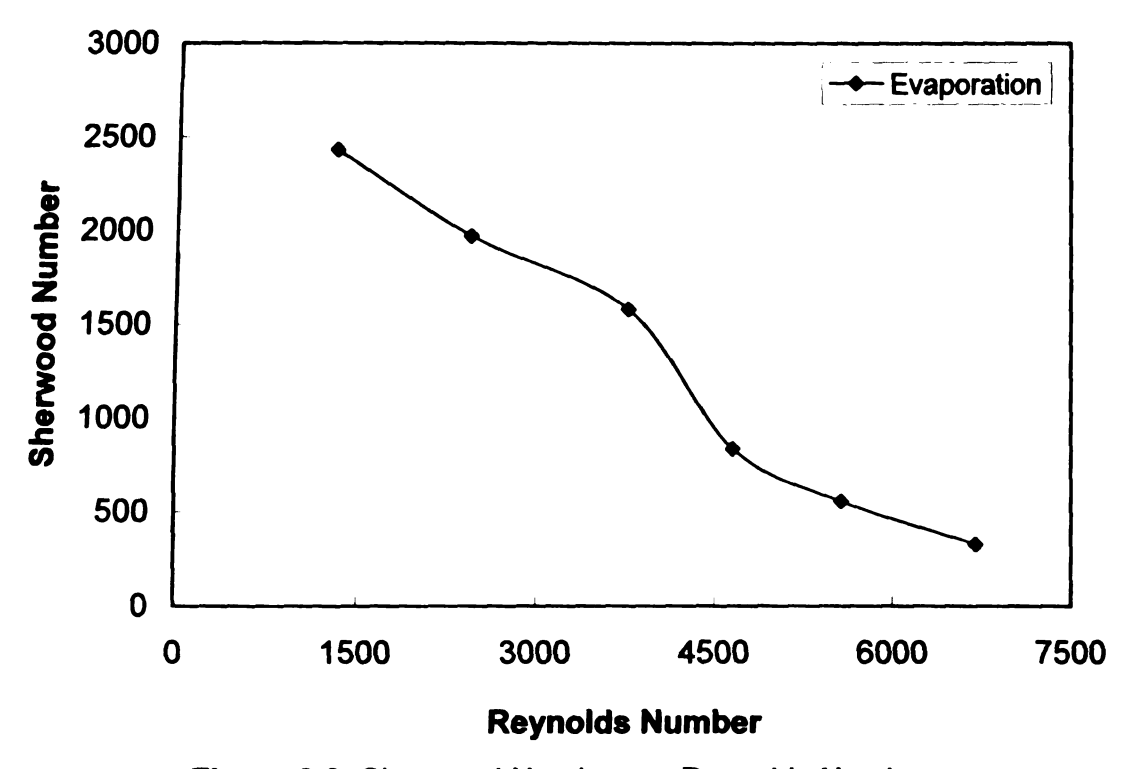
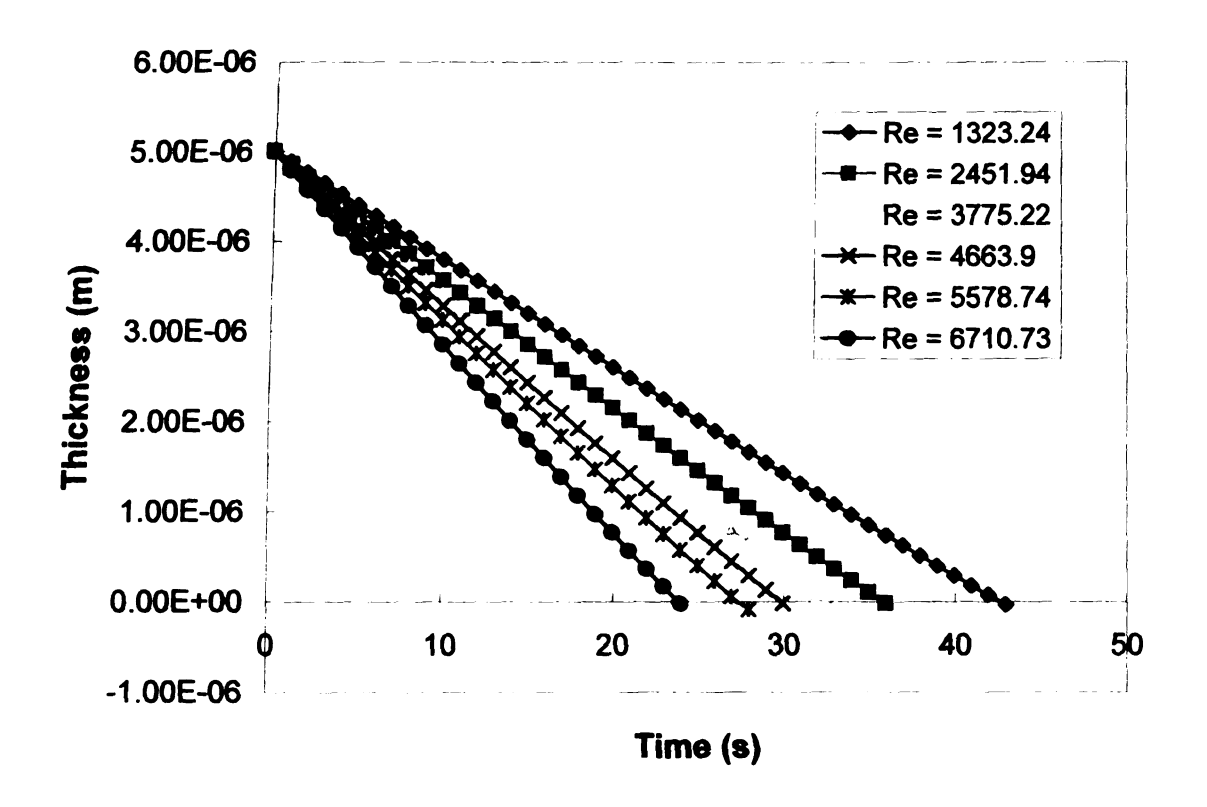


Figure 3.9. Sherwood Number vs. Reynolds Number

Figure 3.10 shows the plot of the liquid layer thickness versus time at different jet Reynolds Number for evaporation. Initially, the boundary layer thickness is set at  $5 \times 10^{-6}$ . For steady state time, it takes between 24 to 43 seconds before the liquid layer thickness reduces to zero. We ran the test at different Reynolds Number by varying the velocity, as higher velocity means higher Reynolds Number. As expected, the plot shows linear lines and all the results have similar trend for different Reynolds Number.



**Figure 3.10.** Liquid Layer Thickness vs. Time at Different Reynolds Number

The assumption of a constant mass transfer coefficient can be investigated by conducting a transient analysis with FLUENT as is done in the next section.

## 3.3 UNSTEADY-STATE INITIAL CONDITION

Since defogging in real automotive world is not as simple as the steady state computational, one must carry out the experimental and computational testing of defogging or defrosting. Previous study provides experimental data that could be used for extensive modeling and prediction of condensation and evaporation for the transient study.

For unsteady-state simulation, the initial condition is similar to what the steady-state simulation are, except that the time is set to unsteady time. The unsteady formulation used is the second-order implicit to obtain more accurate results. The segregated solver makes it possible to solve the governing equations separately. Since the physical properties are assumed to be constant, for the unsteady-state simulation, few different steps were taken to obtain the simulation results.

The initial step taken is selecting flow and turbulent equations, while deselecting the energy equation and the user-defined scalar, in performing the velocity simulation. This step was done until the velocity become converged. During this study, this step becomes converged after 475 iterations.

Once the velocity converged, the second step is to select the energy equation and the user-defined scalar, while deselecting the flow equation in performing the temperature simulation.

These two steps were also taken to save some simulation time. For the steady-state simulation, these steps were not used since the running time is not as long, and the equations were not as complicated as the unsteady-state simulation.

In unsteady-state simulation, there exist a temperature dependent of air at a given pressure, which is the maximum amount of moisture the air can hold. At this point, the air is saturated, and the relative humidity is considered 100%. Any further drop in temperature or addition of moisture results in condensation of water vapor into liquid water in order to keep the thermodynamic equilibrium. The

dew point temperature is defined as the temperature at which condensation begins if the air is cooled at constant pressure. As mixture colds at this constant pressure, the partial pressure of vapor remains constant until the temperature drops below the dew point.

For the unsteady-state simulation, User Defined Function (UDF) [9] was modified in a C program, compiled, and implemented in FLUENT to get the information needed for the mass flux. This UDF also contain the source term needed for the unsteady-state simulation. All operations for the UDF were done via the "define\_adjust" function in the UDF. All the "define\_adjust" functions were used at the beginning of every iteration.

Appendix A and Appendix B shows the UDF used for current transient study. The UDF in Appendix B is similar to that in Appendix A, however it does not contain the mass source of the model. The use of this UDF is to run a simple transient run, hence it will not take as long time to run the computational as UDF with the mass source. However, the accuracy of the result is also less than by using the UDF with mass source.

In both UDF, adjustment of vapor mass fraction is made in the Define\_Adjust function named as spec\_grad. For comparison, local saturation mass fraction of water vapor is stored in user-defined scalar (UDS) in FLUENT. The purpose of storing the flow variables into a user-defined scalar is to get the relative derivatives of the variables that cannot be returned directly by the solver to the UDF but are necessary to specify the source terms needed in the governing equations.

The formula needed to calculate such Reynolds Number, Sherwood Number, condensation rate, evaporation rate, etc should be inputted manually under "Define" pull down menu in FLUENT followed by the Custom Field Function selection. All this extra formula is used for the purpose of post-processing results.

## 3.4 UNSTEADY-STATE RESULTS AND DISCUSSION

For the mass transfer simulation, an ideal gas mixture of vapor and air is set in FLUENT. The mass diffusivity, D, of the vapor in the mixture is assumed to be a constant at  $2.28 \times 10^{-5}$  m<sup>2</sup>/s. The inlet mainstream mass fraction  $\Phi_{\infty}$  corresponding to the relative humidity  $\phi_{\infty}$  can be calculated through the absolute humidity,  $\omega$ . The relationship between absolute humidity and relative humidity is

$$\omega = \frac{0.622\phi P_{sat}}{P - P_{sat}} \tag{3.3}$$

The inlet mass fraction can be calculated from

$$\Phi_{\infty} = \frac{\omega_{\infty}}{1 + \omega_{\infty}} \tag{3.4}$$

The local mass transfer coefficient of vapor along the thermally active plate is of interest of mass transfer, which is defined as

$$h_{m} = \frac{J_{w}}{\rho_{w} - \rho_{\infty}} \tag{3.5}$$

where  $J_w$  is the mass flux at the wall,  $\rho_w$  is the mass concentration at the wall, and  $\rho_\infty$  is the mass concentration along the main stream.

The mass flux itself can be obtained with the following formula

$$J_{w} = -\rho D \left( \frac{\partial \Phi}{\partial y} \right)_{y=0} \tag{3.6}$$

Where D is the mass diffusivity,  $\rho$  is the mixture density of the wall, and  $\Phi$  is the mass fraction of the vapor.

For unsteady-state simulation, the result of the flow field, as expected, is similar to the steady-state simulation. The maximum velocity is slightly lower compared to the steady state velocity. However, the results of transient run are still within 95% confidence interval of previous experimental data. Hence this slight difference could be neglected. This difference could also be a cause of hysteresis. Velocity contour for the unsteady-state simulation is presented in Figure 3.11.1, with the zoom view presented in Figure 3.11.2.

..

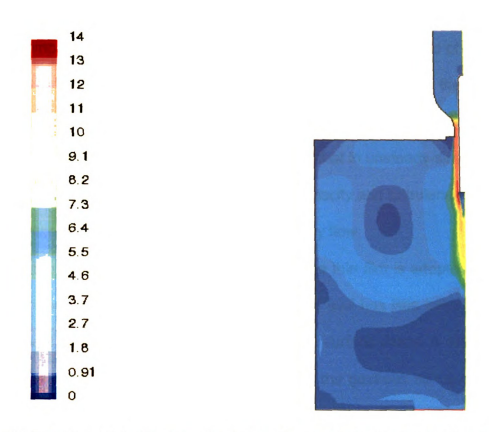


FIGURE 3.11.1. Velocity Flow Field after 5 Seconds In Unsteady-Simulation

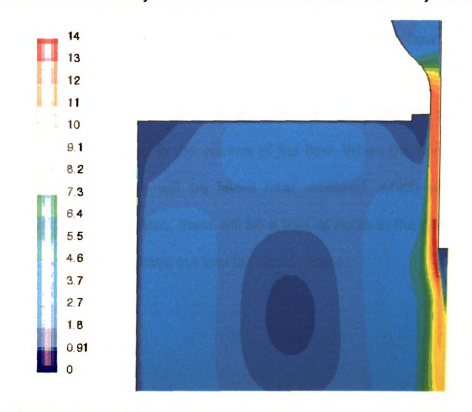
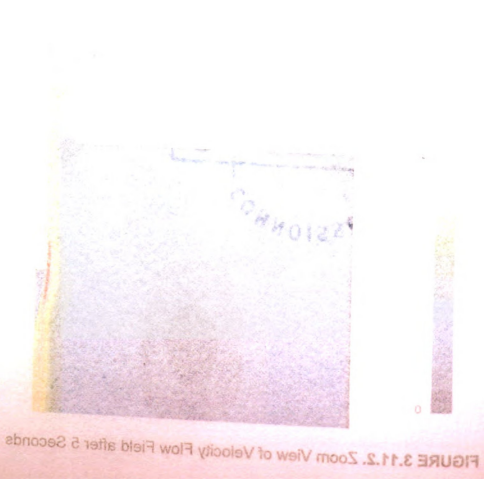


FIGURE 3.11.2. Zoom View of Velocity Flow Field after 5 Seconds



Comparing Figures 3.11.1, 3.11.2 with steady state flow field of air region, Figures 3.1.1, and 3.1.2, the flow field is very similar. Notice that the maximum flow field of air region for the steady-state simulation is slightly higher, but not by much. This higher phenomenon could be caused that in unsteady-simulation, the simulation was done in two steps, by doing the velocity and turbulence first until it reaches steady state, followed by doing the energy flow.

In the volumetric transient model, the same thin film is adopted similar to the 2-D steady state model. The liquid film on the wall has little influence on the velocity field and heat transfer. The impermeable surface model is still assumed valid at the interface between the liquid film and the gaseous air-vapor mixture. The computation starts from the interface where the mass fraction is saturated.

The main difference of transient model with the steady-state model is the possible formation of liquid droplets in the volume of the flow that is now considered. Before, the thermodynamic equilibrium is only maintained on the wall surface. In transient, the water will condense into liquid droplets to keep local thermodynamic equilibrium in the volume of the flow. When the condensation or evaporation occurs, there will be latent heat released, which will affect the temperature distribution. Also, there will be a loss of mass in the gaseous phase as the water vapor condenses out into the liquid phase.

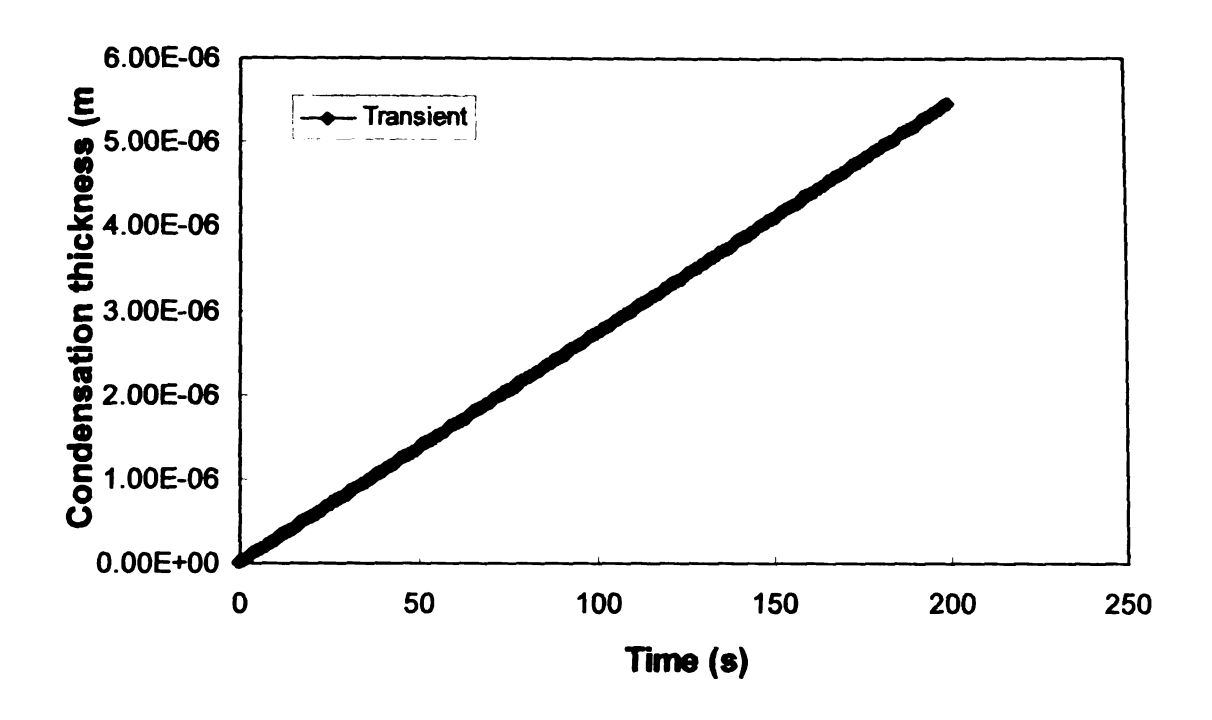


Figure 3.12.1. Present Study of Condensation Thickness vs. Time

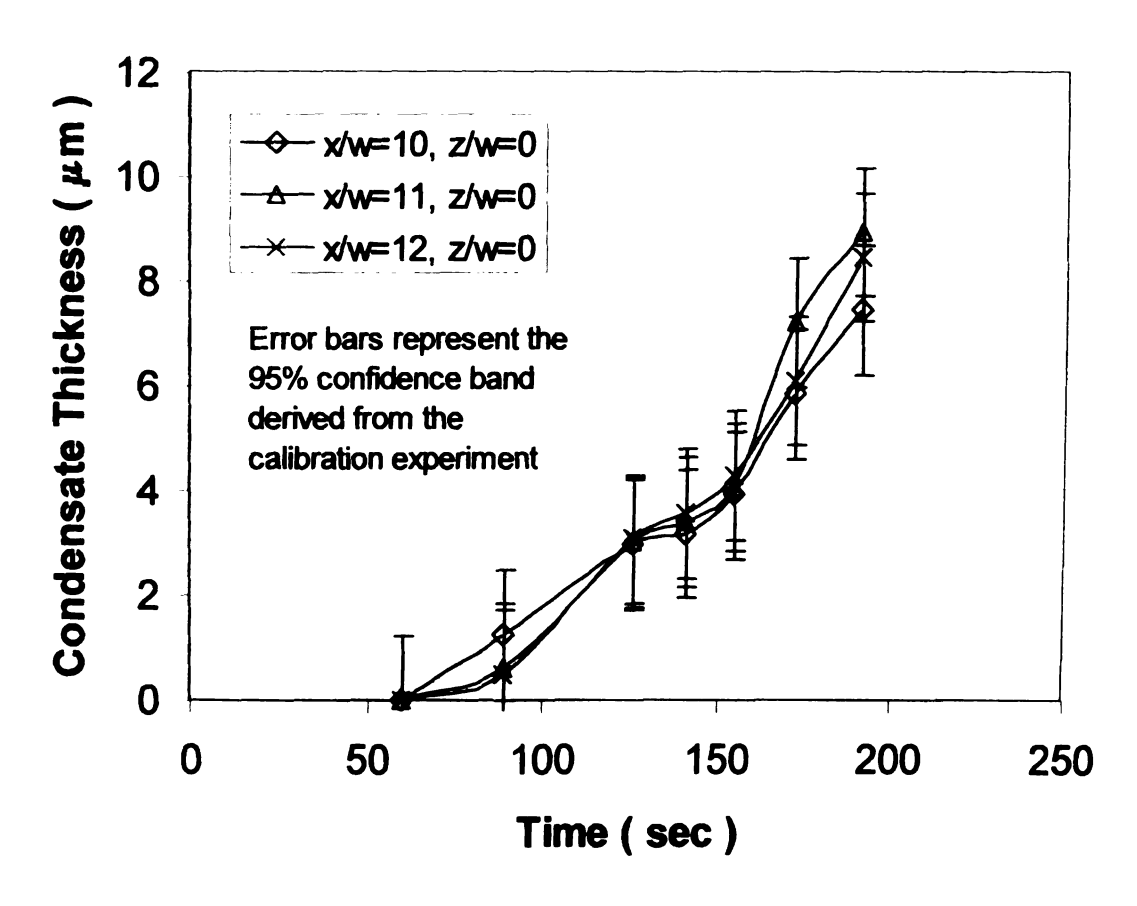


Figure 3.12.2. Condensation Thickness vs. Time from Previous Study

Figure 3.12.1, and 3.12.2 shows the results of condensation thickness versus time from present and previous study respectively. The result of the previous study is obtained from AbdulNour [11]. The present study result shows agreement with the previous study result. Although the numbers of condensation thickness are not exactly the same, the results of the present study are still within 95% confidence bar of the previous study. As expected, condensation thickness for this study should increase linearly, if not almost linearly as time increases during transient run. Though for each x/w the condensation thickness is varying, the plot should show similar trend as seen in Figure 3.12.2.

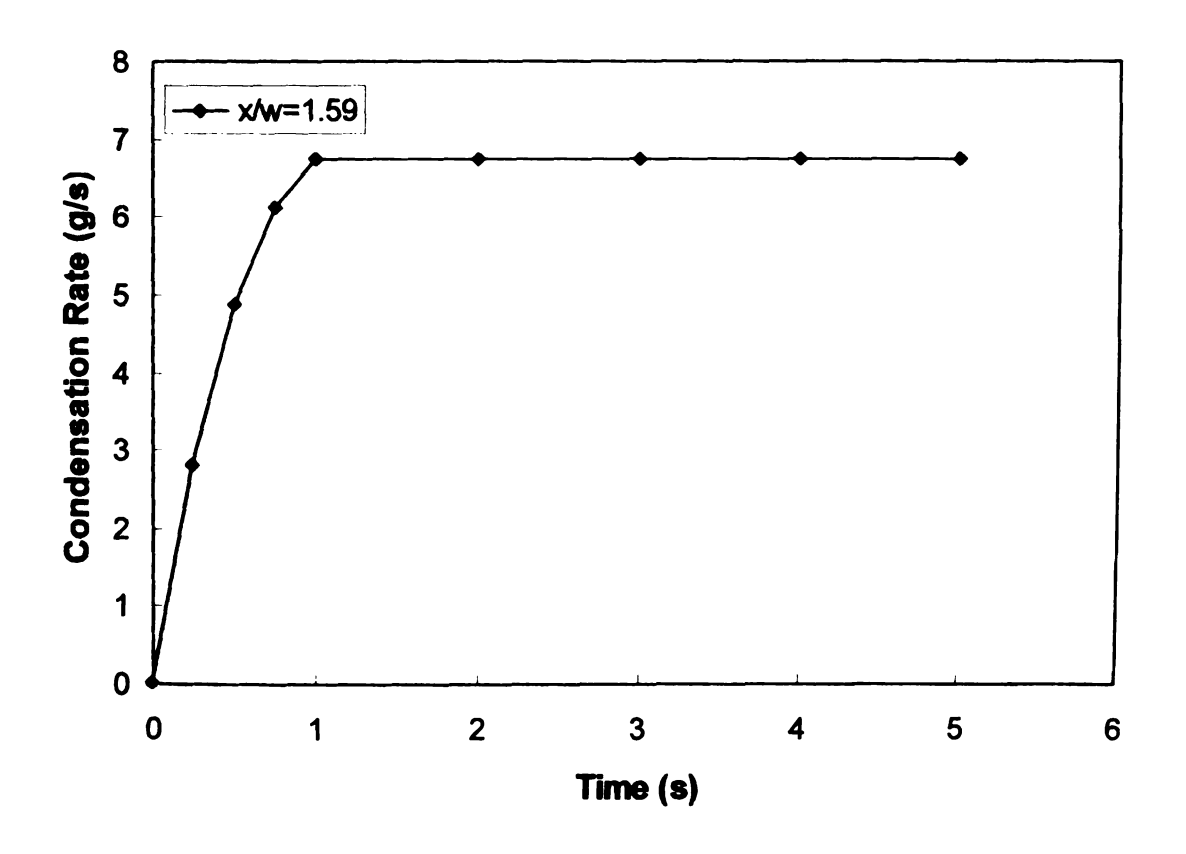


Figure 3.13.1. Mass Flow Rate vs. Time at x/w = 1.59

Figure 3.13.1 above shows the plot mass flow rate against time step at x/w = 1.59. For the transient experiment, each time step is set at 0.25 second for the first four time steps and at increment of one second after that. The maximum iteration per-time step is set at 20. The condensation flow rate after 1 second looks like a straight line, however in the actual data, the flow rate is still increasing in slower rate compared to the first 4 time steps. The flow rate after five seconds become steady state, hence it will just show a straight line. Each x/w location shows similar trend as Figure 3.13.1. However, each x/w has different mass flow rate. The combination plot for the mass flow rate in each x/w is shown in Figure 3.13.2.

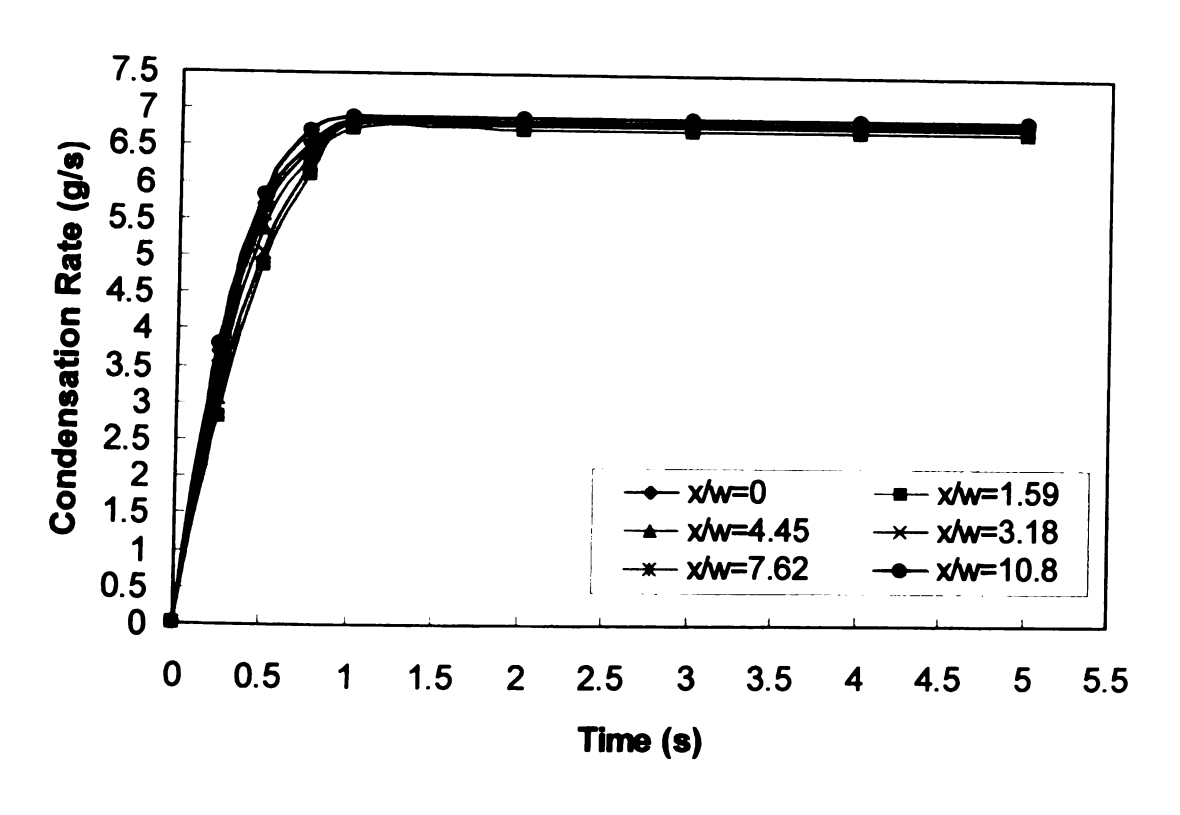


Figure 3.13.2. Mass Flow Rate Vs. Time for Different x/w

The plot of mass flow rate is obtained from the transient condensation experiment instead of the evaporation run.

The plot of each x/w in Figure 3.13.2 after 1 second looks like straight line, however each line actually shows an increasing trend similar to Figure 3.13.1. As observed, as x/w increases, the mass flow rate is also higher with the exception of x/w = 0 where the mass flow rate is higher than the mass flow rate at x/w = 0. This could be a result that at x/w = 0, it is located at the jet nozzle of the model, where the area is smaller than the inlet velocity that causes pressure rise, hence resulting in a high flow rate.

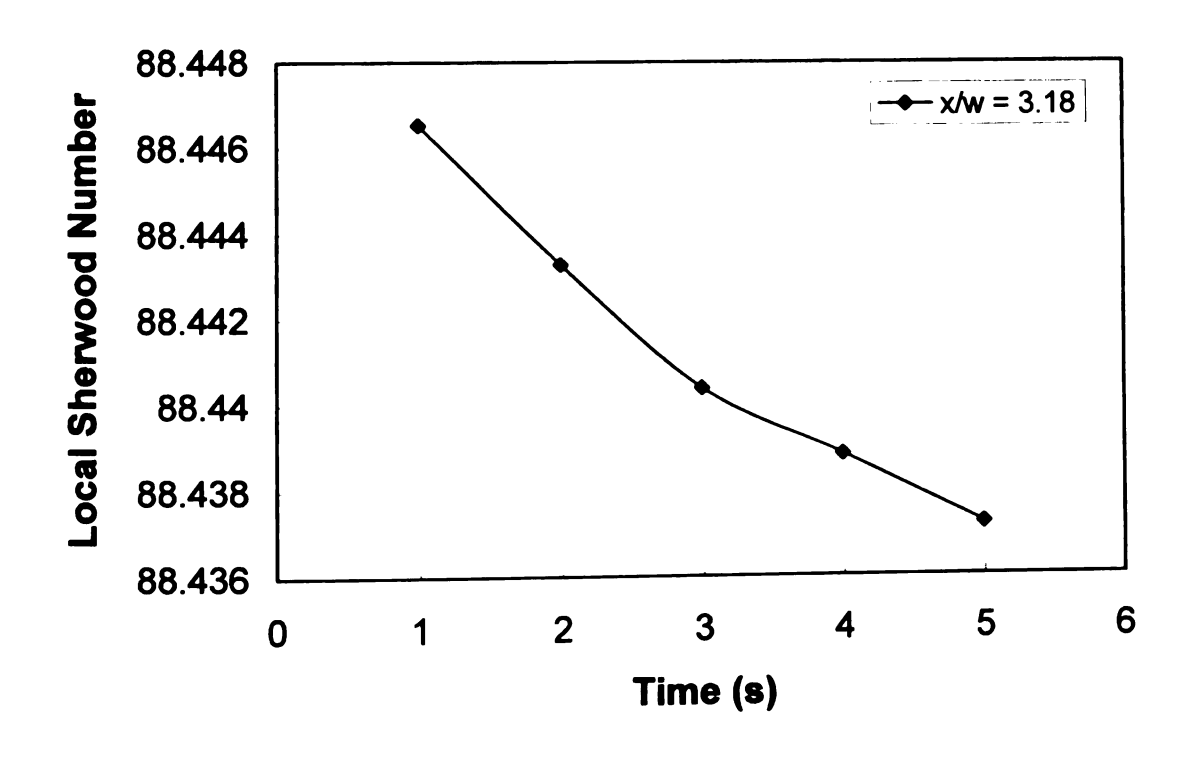


Figure 3.14.1. Local Sherwood Number vs. Time at x/w = 3.18

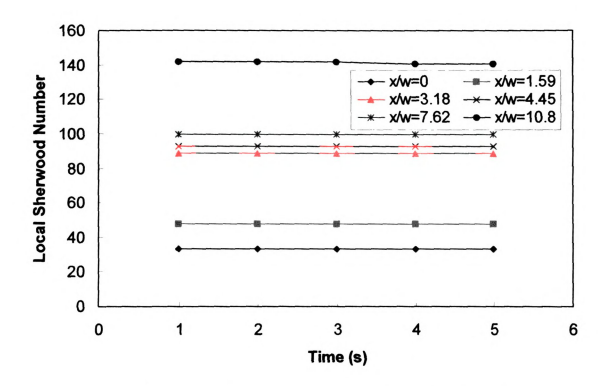


Figure 3.14.2. Local Sherwood Number vs. Time at Different x/w

Figure 3.14.1 presents the Local Reynolds Number versus time at x/w = 3.18. The plot shows that local Sherwood Number is decreasing as time increases. The Sherwood Number will keep decreases as time continues to increase, although the decreasing rate will get slower after certain amount of time. For this transient study, the Sherwood Number is only obtained for some period of time.

The importance of Sherwood Number for this study is to predict the window condensation or evaporation for the automotive industry. If the Sherwood Number of this computational study is in agreement with the experimental study done previously, then in the future the experimental test could be minimized, if

not scrapped, means that minimize the cost of the study by just doing computer simulation.

For all local Sherwood Number versus time for different x/w is presented in Figure 3.14.2. Sherwood Number for each x/w is actually decreasing similar to Figure 3.14.1. The plot in Figure 3.14.2 looks like straight line just because the dimensioning in Microsoft Excel when all local Sherwood Number is plotted in one graph. Results of Sherwood Number versus time in Figure 3.14.2 are internally consistent and in agreement to the experiment results of [1].

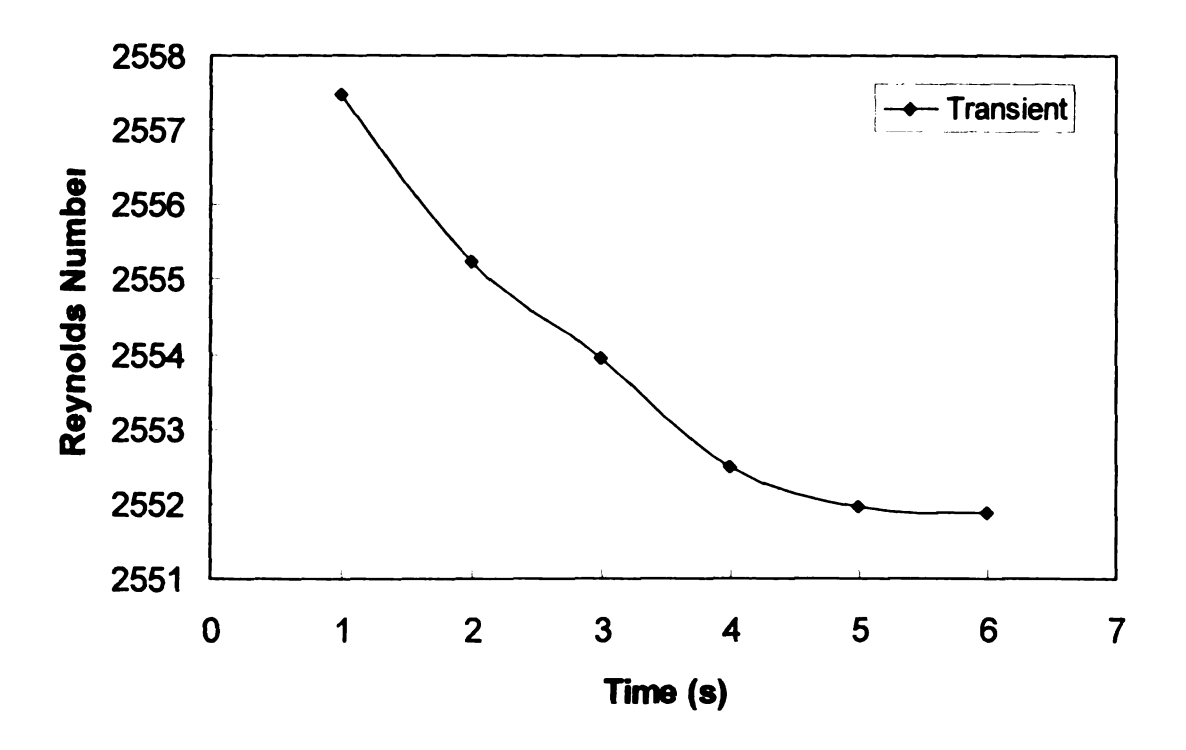


Figure 3.15. Reynolds Number vs. Time

Figure 3.15 presents the plot of Reynolds Number versus time step during a transient run. As mentioned before, each time step is set at one seconds, and

the maximum iteration per-time step is set at 20. As expected, the Reynolds Number is showing a decreasing trend as time step increases, however the decreasing rate will slow down after certain amount of time. The trend of Figure 3.15 is in agreement with the experimental results [1].

Transient computational provides more complex calculation compared to the steady state experiment. In running the iteration it is more complicated since one need to reach steady state first with the velocity and turbulence equation (475 iterations) before running the energy equation to obtained the results expected. With the unsteady time, accurate source term by using UDF is needed in order to run the iteration and not receiving error messages in FLUENT during the iteration run. With the help of FLUENT Support during this study, acceptable results are obtained for the importance of future studies.

From the standpoint of formulation, source terms used are considered to be highly non-linear with respect to the flow variables solved in the governing equations, which make the equations more difficult to solve. The current algorithm of FLUENT is not exactly open to the users, makes it more difficult for user to find out the compatibility of the non-linearity source terms.

#### **CHAPTER 4**

#### CONCLUSIONS AND FUTURE WORK

#### 4.1 CONCLUSIONS

- This study shows that a computational simulation can be applied successfully in order to investigate condensation and evaporation phenomena with excellent comparison to results from previous studies.
- Results of this computational study establish a tool appropriate for the development of defogging analysis.
- It is believed that the volumetric phase change model is in ready stage with theoretical analysis of the model and the source terms to handle the transient problem.
- The transient results are also in agreement with previous studies results.
   Thus a computational study could be done instead of an experimental study, significantly reducing costs.
- Implementation of the UDF into the CFD software package FLUENT is critical in running the transient case, although it is not simple, and could be improved with technical support from FLUENT, Inc.

#### **4.2 FUTURE WORK**

During the development of the study, the author developed several suggestions for future possible improvement. They are summarized below

- One of the shortcomings in the transient study is that the phase change only assumed to be occurred on the wall surface. If further study is done in this part, the author believes more accurate results could be obtained by incorporating moving boundary for the liquid layer.
- Numerically, the limits on velocity, temperature, and vapor concentration conditions in order for the key assumption of the model to hold needs to be further investigated to improve the accuracy of the results.
- Further investigation of compatibility between the algorithm of the code and the highly nonlinear source terms would also be of interest.
- More parameters could be investigated for the transient run, e.g. varying the velocity, temperature, concentration potential, and other basic initial conditions to capture all possible condition of window defogging or defrosting in the real world.
- Impact of flow transition from laminar to turbulent flow might be an interest for future study subject, since it will have some effect in the calculation accuracy of the model.
- With the development of FLUENT software, there is always room for improvement for the transient study in predicting window defogging or defrosting with or without UDF.

- The liquid layer set for current study is adiabatic. More sophisticated
  model for liquid layer with the effect of the outside part of the windshield
  could be an interest for future study.
- Further experimental test could be done with different Reynolds Number by using the valid Sherwood Number obtained in current study. Though this may change the geometry of the model.

## **APPENDICES**

## **APPENDIX A**

## USER DEFINED FUNCTION FOR THE VOLUMETRIC PHASE CHANGE MODEL

```
#include "udf.h"
#include "sg.h"
#define L 2400.0e3 /* latent heat of water [J/kg] */
#define b L*18 / 8314.4
#define a b / (273.15 + 100.)
DEFINE_ADJUST(spec_grad, domain)
{
   Thread *t;
   cell tc:
   face tf:
   float MLFS; /* saturation mole fraction */
   float MSFS; /* saturation mass fraction */
   float UVPR; /* x velocity of vapor */
   float VVPR; /* y velocity of vapor */
   thread_loop_c (t,domain)
       begin c loop all (c,t)
           MLFS = exp(a - b / C_T(c,t));
              /* equation (4.23) */
           MSFS = (MLFS * 18./29.) / (1. - MLFS * 18./29.) / (1. - MLFS * 18./29.)
          (1. - 18./29.));
              /* equation (4.24) */
          if (C_YI(c,t,0) > MSFS) C_YI(c,t,0) = MSFS;
          if (C YI(c,t,0) \le 0.0)
              C YI(c.t.0) = 1.0e-12:
          /* adjust the mass fraction of vapor if its is
          higher than the saturation value. */
          if (NULL != THREAD STORAGE(t,SV_UDS_I(3)) &&
              NULL != THREAD STORAGE(t,SV UDS I(0)))
          {
```

```
C_UDSI(c,t,3) = MSFS;
                C\_UDSI(c,t,0) = C\_YI(c,t,0);
            }
        end_c_loop_all (c,t)
 }
 thread_loop_f (t,domain)
    if (NULL != THREAD_STORAGE(t,SV_UDS_I(3)) &&
        NULL != THREAD_STORAGE(t,SV_UDS_I(0)))
    {
        begin_f_loop (f,t)
        {
           float FMLFS = \exp(a - b / F_T(f,t));
           float FMSFS = (FMLFS * 18./29.) /
           (1. - FMLFS * (1. - 18./29.));
           F_UDSI(f,t,3) = FMSFS;
           F_UDSI(f,t,0) = F_YI(f,t,0);
       end_f_loop (f,t)
   }
}
thread_loop_c (t,domain)
   if (NULL != THREAD_STORAGE(t,SV_UDS_I(0)) &&
       NULL != T_STORAGE_R_NV(t,SV_UDSI_G(0)))
   {
       begin_c_loop_all (c,t)
       {
          float diff eff = 2.88e-5 +
                         (C_MU_T(c,t)/0.7);
          UVPR = C_U(c,t) - diff_eff *
              C_UDSI_G(c,t,0)[0]/C_UDSI(c,t,0);
          VVPR = C_V(c,t) - diff_eff *
              C UDSI_G(c,t,0)[1]/C_UDSI(c,t,0);
          C_UDSI(c,t,1) = C_R(c,t) * C_UDSI(c,t,0)
                      * UVPR:
          C_UDSI(c,t,2) = C_R(c,t) * C_UDSI(c,t,0)
                     * WPR:
      end_c_loop_all (c,t)
```

```
}
 }
 thread_loop_f (t,domain)
 /* assign face value with way (1) */
     if (NULL != THREAD_STORAGE(t,SV_UDS_I(0)) &&
        NULL != THREAD_STORAGE(t,SV_UDS_I(1)) &&
        NULL != THREAD_STORAGE(t,SV_UDS_I(2)))
     {
        begin_f_loop (f,t)
            cell_t cell = F CO(f,t);
            Thread *c_thread = THREAD_T0(t);
            if (NULL !=
            T_STORAGE_R_NV(c_thread,SV_UDSI_G(0)))
            {
               F UDSI(f,t,1) =
                       C_UDSI(cell,c_thread,1);
               F_UDSI(f,t,2) =
                      C_UDSI(cell,c thread,2);
            }
         end_f_loop (f,t)
      }
   }
}
DEFINE_PROFILE(plate_mf, t, position)
/* specify saturation mass fraction at the boundary */
{
   face tf;
   begin_f loop (f,t)
   {
       float FMLFS = \exp(a - b / F T(f,t));
       F_PROFILE(f,t,position) = (FMLFS * 18./29.) /
                      (1. - FMLFS * (1. - 18./29.));
   end_f_loop (f,t)
}
DEFINE_SOURCE(mass_src, c, t, dS, eqn)
/* source term of continuity and concentration equation */
{
 float source;
```

```
if (NULL != T_STORAGE_R_NV(t,SV_UDSI_G(1)) &&
         NULL != T_STORAGE_R_NV(t,SV_UDSI_G(2)) &&
         NULL != THREAD_STORAGE(t,SV_UDS_I(0)) &&
         NULL != THREAD_STORAGE(t,SV_UDS_I(3)))
         if (C\_UDSI(c,t,0) < C\_UDSI(c,t,3))
            source = 0.;
         else
            source = C_UDSI_G(c,t,1)[0] +
                  C_UDSI_G(c,t,2)[1];
              /* equation (4.34) */
 dS[eqn]=0;
 return source;
DEFINE_SOURCE(energy_src, c, t, dS, eqn)
/* source term for energy equation */
 float source;
   if (NULL != T_STORAGE_R_NV(t,SV_UDSI_G(1)) &&
        NULL != T_STORAGE_R_NV(t,SV_UDSI_G(2)) &&
        NULL != THREAD_STORAGE(t,SV_UDS_I(0)) &&
        NULL != THREAD_STORAGE(t,SV_UDS_I(3)))
    {
        if (C\_UDSI(c,t,0) < C\_UDSI(c,t,3))
           source = 0:
        else
           source = -L * (C_UDSI_G(c,t,1)[0] +
C_UDSI_G(c,t,2)[1]);
 dS[eqn]=0;
 return source;
```

## **APPENDIX B**

# USER DEFINED FUNCTION FOR THE VOLUMETRIC PHASE CHANGE MODEL (WITHOUT MASS SOURCE)

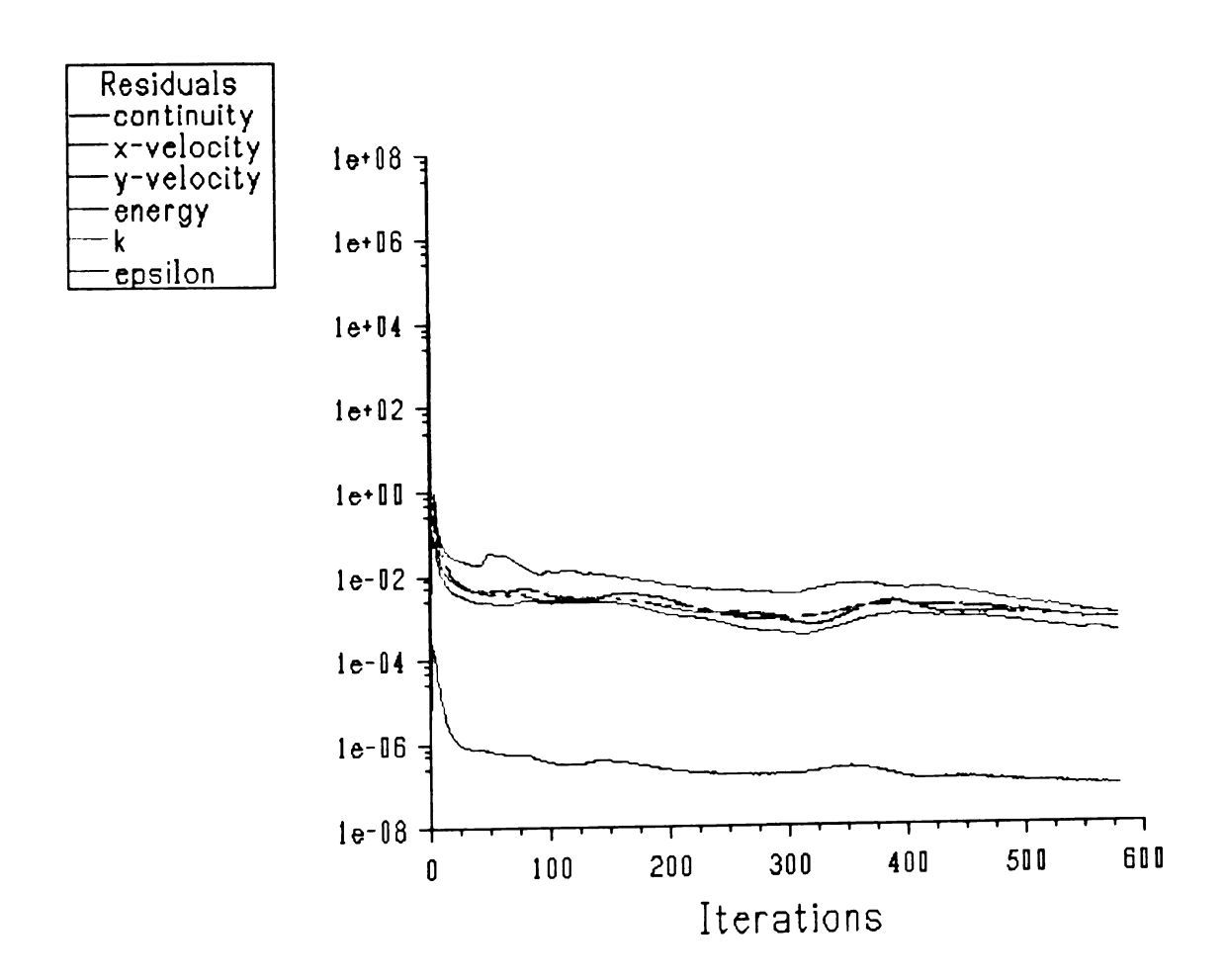
```
#include "udf.h"
#include "sg.h"
#define L 2400.0e3 /* latent heat of water [J/kg] */
#define b L*18 / 8314.4
#define a b / (273.15 + 100.)
DEFINE_ADJUST(spec_grad, domain)
   Thread *t;
   cell tc:
   face tf;
   float MLFS; /* saturation mole fraction */
   float MSFS; /* saturation mass fraction */
   float UVPR; /* x velocity of vapor */
   float VVPR; /* y velocity of vapor */
   thread_loop_c (t,domain)
   {
       begin_c_loop_all (c,t)
       {
           MLFS = \exp(a - b / C_T(c,t));
              /* equation (4.23) */
           MSFS = (MLFS * 18./29.) / (1. - MLFS * 18./29.) / (1. - MLFS * 18./29.)
           (1. - 18./29.));
              /* equation (4.24) */
          if (C_Y|(c,t,0) > MSFS) C Y|(c,t,0) = MSFS;
          if (C_YI(c,t,0) \le 0.0)
              C YI(c,t,0) = 1.0e-12:
          /* adjust the mass fraction of vapor if its is
          higher than the saturation value. */
          if (NULL != THREAD STORAGE(t,SV UDS I(3)) &&
              NULL != THREAD STORAGE(t,SV UDS I(0)))
          {
```

```
C_UDSI(c,t,3) = MSFS;
                C\_UDSI(c,t,0) = C\_YI(c,t,0);
            }
        end_c_loop_all (c,t)
 }
 thread_loop_f (t,domain)
    if (NULL != THREAD_STORAGE(t,SV_UDS_I(3)) &&
        NULL != THREAD_STORAGE(t,SV_UDS_I(0)))
    {
        begin_f_loop (f,t)
       {
           float FMLFS = exp(a - b / F_T(f,t));
           float FMSFS = (FMLFS * 18./29.) /
           (1. - FMLFS * (1. - 18./29.));
           F_UDSI(f,t,3) = FMSFS;
           F_UDSI(f,t,0) = F_YI(f,t,0);
       end_f_loop (f,t)
   }
}
thread_loop_c (t,domain)
{
   if (NULL != THREAD_STORAGE(t,SV_UDS_I(0)) &&
       NULL != T_STORAGE_R_NV(t,SV_UDSI_G(0)))
       begin_c_loop_all (c,t)
       {
          float diff eff = 2.88e-5 +
                         (C_MU_T(c,t)/0.7);
          UVPR = C U(c,t) - diff_eff *
              C_UDSI_G(c,t,0)[0]/C_UDSI(c,t,0);
          VVPR = C V(c,t) - diff eff *
              C_UDSI_G(c,t,0)[1]/C_UDSI(c,t,0);
          C_UDSI(c,t,1) = C_R(c,t) * C_UDSI(c,t,0)
                      * UVPR:
          C_UDSI(c,t,2) = C_R(c,t) * C_UDSI(c,t,0)
                     * VVPR;
      end_c_loop_all (c,t)
```

```
}
}
thread_loop_f (t,domain)
/* assign face value with way (1) */
    if (NULL != THREAD_STORAGE(t,SV UDS I(0)) &&
        NULL != THREAD_STORAGE(t,SV_UDS_I(1)) &&
        NULL != THREAD_STORAGE(t,SV_UDS_I(2)))
    {
        begin f loop (f,t)
           cell_t cell = F_C0(f,t);
           Thread *c_thread = THREAD_T0(t);
           if (NULL !=
           T_STORAGE_R_NV(c_thread,SV_UDSI_G(0)))
               F_UDSI(f,t,1) =
                      C UDSI(cell,c thread,1);
               F_UDSI(f,t,2) =
                      C_UDSI(cell,c_thread,2);
           }
        end_f_loop (f,t)
   }
}
DEFINE_PROFILE(plate_mf, t, position)
/* specify saturation mass fraction at the boundary */
{
   face tf;
   begin_f_loop (f,t)
       float FMLFS = exp(a - b / F_T(f,t));
       F_PROFILE(f,t,position) = (FMLFS * 18./29.) /
                      (1. - FMLFS * (1. - 18./29.));
   }
   end_f_loop (f,t)
}
DEFINE_SOURCE(energy_src, c, t, dS, eqn)
/* source term for energy equation */
 float source;
```

**APPENDIX C** 

## **RESIDUAL PLOT OF 2-D STEADY STATE RUN**



## **APPENDIX D**

## **COMPUTATIONAL RESULTS**

Table D.1. Condensation Rate with Only Diffusion

Δconcentration	M (g/min)
0.0044192	0.279067
0.00476326	0.286247
0.00514243	0.295807
0.00560799	0.307826
0.00615095	0.322712
0.00675215	0.341049
0.00744845	0.362481
0.0082635	0.39361
0.00921561	0.436279
0.0103052	0.488144
0.0115558	0.552178
0.0130065	0.628601
0.0146356	0.730184
0.0164875	0.864014
0.0185547	1.01902

Table D.2. Condensation Rate with Only Convection

△concentration	M (g/min)
0.0044192	0.096576
0.00476326	0.104663
0.00514243	0.114017
0.00560799	0.125301
0.00615095	0.1376
0.00675215	0.158679
0.00744845	0.191277
0.0082635	0.225842
0.00921561	0.264279
0.0103052	0.309194
0.0115558	0.373768
0.0130065	0.466739
0.0146356	0.561326
0.0164875	0.657306
0.0185547	0.76371

Table D.3. Condensation Rate with Convection and Diffusion

△concentration M (g/m	
0.0044192	0.479285

0.00476326	0.491614
0.00514243	0.508035
0.00560799	0.528677
0.00615095	0.554242
0.00675215	0.585735
0.00744845	0.622543
0.0082635	0.676006
0.00921561	0.749288
0.0103052	0.838363
0.0115558	0.948339
0.0130065	1.07959
0.0146356	1.25405
0.0164875	1.4839
0.0185547	1.75012

Table D.4. Reynolds and Sherwood Number for Condensation

Reynolds	Sherwood
920.4194	3950.16
1490.928	3981.3
2120.237	2650.97
2760.184	1304.03
4250.244	592.781
5440.826	469.35

Table D.5. Reynolds and Sherwood Number for Evaporation

Reynolds	Sherwood
1323.24	4973.98
2451.94	4896.83
3775.22	3017.72
4663.9	1469.95
5578.74	646.939
6710.73	466.2579

Table D.6. Reynolds Number for Transient

Time (s)	Re#
1	2557.474
2	2555.223
3	2553.944
4	2552.483
5	2551.953
6	2551.858

Table D.7. Liquid Layer Thickness vs. Time for Different Reynolds Number

	Re=1323.24	
0	0.000	5.00E-06

5	4.337	4.34E-06
10	3.344	3.34E-06
15	2.197	2.20E-06
20	9.657	9.66E-07
25	4.765	4.77E-07
30	2.566	2.57E-07
35	9.654	9.65E-08
40	5.674	5.67E-08
45	2.902	2.90E-08
50	1.241	1.24E-08
55	0.936	9.36E-09
60	0.750	7.50E-09
64	0.000	0.00E+00

	Re=2451.94	
0	0.000	5.00E-06
5	3.686	3.69E-06
10	2.842	2.84E-06
15	1.867	1.87E-06
20	8.208	8.21E-07
25	4.051	4.05E-07
30	2.181	2.18E-07
35	8.206	8.21E-08
40	4.823	4.82E-08
45	2.466	2.47E-08
50	1.055	1.05E-08
55	0.795	7.95E-09
60	0.000	0.00E+00

	Re=3775.22	
0	0.000	5.00E-06
5	3.252	3.25E-06
10	2.508	2.51E-06
15	1.648	1.65E-06
20	7.243	7.24E-07
25	3.574	3.57E-07
30	1.924	1.92E-07
35	7.241	7.24E-08
40	4.256	4.26E-08
45	2.176	2.18E-08
50	0.931	9.31E-09

55	0.702	7.02E-09
56	0.000	0.00E+00

	Re=4663.90	
0	0.000	5.00E-06
5	2.819	2.82E-06
10	2.173	2.17E-06
15	1.428	1.43E-06
20	6.277	6.28E-07
25	3.098	3.10E-07
30	1.668	1.67E-07
35	6.275	6.28E-08
40	3.688	3.69E-08
45	1.886	1.89E-08
50	0.807	8.07E-09
52	0.000	0.00E+00

	Re=5578.74	
0	0.000	5.00E-06
5	2.385	2.39E-06
10	1.839	1.84E-06
15	1.208	1.21E-06
20	5.311	5.31E-07
25	2.621	2.62E-07
30	1.411	1.41E-07
35	5.310	5.31E-08
40	3.121	3.12E-09
45	1.596	1.60E-09
46	0.000	0.00E+00

	Re=6710.73	
0	0.000	5.00E-06
5	1.951	1.95E-06
10	1.505	1.50E-06
15	7.243	7.24E-07
20	2.144	2.14E-07
25	1.155	1.15E-07
30	4.344	4.34E-08
35	2.553	2.55E-08
40	1.306	1.31E-08
42	0.000	0.00E+00

**BIBLIOGRAPHY** 

## **Bibliography**

- [1] Hoke, P. B. (2001). Experimental Study of Heat Transfer and Phase Change Condensation in a Developing, Two-Dimensional Wall Jet Flow Field with an Isothermal Boundary Condition, Thesis for PhD. Degree, Department of Mechanical Engineering, Michigan State University
- [2] Launder, B. E. and Rodi, W. (1981). *The Turbulent Wall Jet*, Prog. Aerospace Sci., Vol. 19, pp. 81-128.
- [3] Legay-Desesquelles, F. and Prunet-Foch, B. (1986). Heat and Mass Transfer with Condensation in Laminar and Turbulent Boundary Layers along a Flat Plate, Int. J. Heat Mass Transfer, Vol. 29, No 1, pp. 95-105.
- [4] AbdulNour, B. S. (1998). *CFD Simulation of a Model Wall Jet Flow for Defogging and Defrosting*, Project Report Corporation. Visteon, Michigan.
- [5] AbdulNour, R. S., Willenborg, K., McGrath, J. J., Foss, J. F., AbdulNour, B. S. (2000). *Measurement of the Convection Heat Transfer Coefficient for a Planar Wall Jet: Uniform Temperature and Uniform Heat Flux Boundary Conditions*, Exper. Therm. Fluid Sci., Vol. 22, No. 3, pp. 123-131.
- [6] Peterson, P. F. (2000). *Diffusion Layer Modeling for Condensation with Multi-Components Non-Condensable Gases*, Journal of Heat Transfer Trans. ASME, Vol. 122, No. 4, pp. 716-720.
- [7] Siow, E. C., Ormistion, S. J., Soliman, H. M. (2002). Fully Coupled Solution of a Two-Phase Model for Laminar Film Condensation of Vapor-Gas Mixtures in Horizontal Channels, Int. J. Heat and Mass Transfer, Vol. 45, No. 18, pp. 3689-3702.
- [8] Hassan, M. B., Petitjean, C., Deffieux, J. C., Gilotte, P. (1999). Windshield Defogging Simulation with Comparison to Test Data, Society of Automotive Engineers, Inc., Valeo Thermique Habitacle.
- [9] Wang, Qingtian (1999). Numerical Simulations of a Developing Turbulent Wall Jet Along a Thermally Active Surface, Thesis for Master Degree, Department of Mechanical Engineering, Michigan State University.
- [10] FLUENT Incorporated (2001). FLUENT 6 User's Guide.
- [11] AbdulNour, B. S. (2000). *Prediction of Fogging and Demisting*, Project Presentation. Visteon Corporation, Michigan.

- [12] AbdulNour, B. S. (1998). *Numerical Simulation of Vehicle Defroster Flow Field*, Automotive Climate Control, SAE Publication SP-1347, SAE Paper No. 980285, pp.9-14.
- [13] Cengel, Y. A. and Boles, M. A. (1989). <u>Thermodynamics An Engineering Approach</u>, McGraw-Hill, Inc.
- [14] Eriksson, J. G., Karlsson, R. I. and Persson, J. (1998). *An Experimental Study of aTwo-Dimensional Plane Turbulent Wall Jet*, Experiments in Fluids 25, pp. 50-60.
- [15] Mills, A. F. (1999). <u>Basic Heat and Mass Transfer</u>, 2<sup>nd</sup> Edition, Prentice Hall, Inc., New Jersey.
- [16] Incorpera, F. P., and Dewitt, D. P. (1996). <u>Fundamentals of Heat and Mass Transfer</u>, 4<sup>th</sup> Edition, John Wiley and Sons, New York.
- [17] Anderson, D. A., Tannehill, J. C., and Pletcher, R. H. (1984). <u>Computational Fluid Mechanics and Heat Transfer</u>, Taylor and Francis, Washington D.C.
- [18] Versteeg, H. K., Malalasekera, W. (1995). <u>An Introduction to Computational Fluid Dynamics</u>, The Finite Volume Method, John Wiley and Sons, New York.
- [19] Hoke, P. B., Wang, Q., McGrath, J. J., AbdulNour, B. S. (1999). Experimental and Numerical Study of a Condensing Flow in a Developing Wall Jet, Turbulent Shear Flow Phenomena – 1 Conference, Santa Barbara CA, pp. 391-396.
- [20] Goldstein, R. J., and Cho, H. H. (1995). A Review of Mass-Transfer Measurements Using Naphthalene Sublimation, Experimental Thermal and Fluid Science, Vol. 10, Iss. 4, pp. 416 434.
- [21] Goldstein, R. J. (1996). <u>Fluid Mechanics Measurement, 2<sup>nd</sup> Edition</u>, Taylor and Francis, Washington D.C.